2011

V2O5-WO3 composite films and surface-coated LiCoO2 for enhanced Li-ion intercalation properties

Chuan Cai
Louisiana State University and Agricultural and Mechanical College, ccai1@tigers.lsu.edu

V_2O_5-WO_3 COMPOSITE FILMS AND SURFACE-COATED $LiCoO_2$ FOR ENHANCED Li-ION INTERCALATION PROPERTIES

A Thesis

Submitted to the Graduate Faculty of the
Louisiana State University and
Agricultural and Mechanical College
in partial fulfillment of the
requirements for the degree of
Master of Science in Mechanical Engineering

in

The Department of Mechanical Engineering

By
Chuan Cai
B.S., University of Science and Technology of China, Hefei, China, 2008
May 2011

Acknowledgements

First and foremost, I would like to express my deepest appreciation to Dr. Ying Wang, my major professor. It is her who provides this chance for me to work on this project. Her guidance, patience and encouragement help me to improve my academic knowledge and experimental skills. I am also grateful to Dr. Dorel Moldovan, Dr. Shengmin Guo and Dr. Wenjin Meng for their time and assistance. Moreover, I would like to thank my labmate Dongsheng Guan for his advice on research and in life. Finally, I would like to thank my parents for their love and encouragement.

Table of Contents

List of Figures

Abstract

We have investigated the enhanced Li-ion intercalation properties of two different materials, which are V_2O_5-WO_3 composite and surface-coated $LiCoO_2$. A simple and novel solution processing method is employed to prepare V_2O_5-WO_3 composite films that demonstrate enhanced Li-ion intercalation properties for applications in Li-ion batteries or electrochromic displays. This solution processing method employs precursors that only contain the elements of V, W, O and H, which avoids impurity elements such as Na that has been commonly used in other solution methods (e.g. using precursors of sodium metavanadate and sodium tungstate solution). The V_2O_5-WO_3 composite films show enhanced Li-ion intercalation properties compared to pure V_2O_5 and WO_3 films. For example, at a high current density of 1.33 A/g, the V_2O_5-WO_3 film with a V_2O_5/WO_3 molar ratio of 10/1 exhibits the highest discharge capacities of 200 mA•h/g at the first cycle and 132 mA•h/g after 50 cycles, while pure V_2O_5 film delivers discharge capacities of 108 mA•h/g at the first cycle and 122 mA•h/g after 50 cycles. The enhanced capacity of the composite films is ascribed to the reduced crystallinity, increased porosity and thus the enhanced surface area. Both cyclic voltammogram and chronopotentiometric curves of the V_2O_5-WO_3 film with a molar ratio of 10:1 are distinctively different from those of pure oxide films, suggesting a different Li-ion intercalation process in the V_2O_5-WO_3 film with the molar ratio of 10:1.

For surface-coated $LiCoO_2$, a molten salt synthesis method is employed to prepare $LiCoO_2$ powders with submicron size, and ultrathin conformal Al_2O_3 or ZnO

layers are coated on $LiCoO_2$ electrodes by utilizing atomic layer deposition. The Al_2O_3-coated $LiCoO_2$ electrode exhibits improve cycling stability during the electrochemical measurements, while the ZnO-coated $LiCoO_2$ electrode does not show an improved cycling performance. The Al_2O_3 coating can prevent the direct contact between $LiCoO_2$ and the electrolyte, and thus suppress the cobalt dissolution and side reaction. Therefore, $LiCoO_2$ with nanosized thin Al_2O_3 coating exhibits improved cycling performance. In contrast, the ZnO coating is not electrochemically stable, so the ZnO-coated $LiCoO_2$ electrode exhibits a similar cycling performance with the bare $LiCoO_2$ electrode.

Chapter1 Introduction

1.1 General Background

With the shortage of fossil fuels and associated price increases, it is more and more urgent to find new energy sources to alleviate the increasing pressure on an already stretched world energy infrastructure. Renewable energy technologies such as solar cells, fuel cells, and bio-fuels have achieved significant progress, although these energy sources had been marginalized before. It is expected that oil and gasoline will not serve as our primary fuel in the coming decades when alternative energy sources are more practical and price competitive. However, the renewable energy technologies have not reached widespread use up until now, because they are limited by the properties of the materials in the designed sophisticated device structures. For example, poor charge and mass transport properties significantly limit the energy and power density in portable electric power sources. The energy conversion efficiency of organic photovoltaic cells is less than 6% due to poor charge carrier mobilities in organic/polymer semiconductors [1]. More efficient energy conversion devices and high-density energy/power storage can be achieved by utilizing new materials that are chemically modified through molecular or atomic engineering and/or possess unique microstructures.

Electrochemical energy storage and conversion has been considered seriously as one alternative energy/power source, as long as this energy consumption will be more sustainable and more environmentally benign. Li-ion batteries are a representative system for such electrochemical energy production. At present, Li-ion batteries are

widely used in portable electronic devices such as laptop computers, digital cameras and cellular phones due to their high efficiency, light weight and rechargeable property [2]. Moreover, they have been intensively studied as power supplies in devices requiring high energy and high power densities such as electric vehicles (EVs) and hybrid electric vehicles (HEVs). However, the power density of Li-ion batteries is relatively low especially at high charging-discharging rates in despite of the high energy density [3]. The low power density is ascribed to a large polarization caused by slow lithium diffusion in the active material and high resistance in the electrolyte. In addition, the dissolution of electrode materials and resulting structure change deteriorate the cycling performances of the Li-ion batteries. To overcome these problems, it is important to design and fabricate composite electrode materials with electrochemically stable structures, enhanced ionic transport and electronic conduction.

1.2 Lithium-Ion Batteries

An electrochemical battery, mainly composed of an anode, a cathode, and an electrolyte, converts chemical potential to electric energy through Faradaic reactions. These reactions including heterogeneous charge transfer occur at the surface of an electrode [4]. The electrochemical batteries are broadly divided into two groups: primary batteries that are single-use devices and cannot be recharged; secondary batteries that are also called rechargeable batteries and can be recharged many times. For typical energy storage in a secondary battery, faradaic reactions take place at the surface of an electrode, and mass and charge transfer through the electrode. Therefore,

the performance of the battery depends on the surface area and the transport distance. Moreover, the surface reaction, transfer processes and their cyclic stability are significantly influenced by chemical composition, crystal structure, and microstructure.

Intercalation electrodes in batteries consist of electrochemically active materials that serve as a host solid. Guest species such as Li ions from an electrolyte can intercalate into the host solid reversibly. Intercalation compounds are a special family of materials. This kind of materials provide a crystalline host lattice that contains an interconnected system of empty lattice sites with appropriate size, and mobile guest species (atoms, molecules or ions) can intercalate into the lattice reversibly without destroying the structural integrity of host lattice [5]. It has been found that the intercalation reactions occur in various host lattice structures around room temperature [6]. Layered host lattices have high structural flexibility and are able to adapt the geometry of the intercalated guest species by free adjustment of the interlayer separation. All the layer hosts are characterized by strong interlayer covalent bonding and weak interlayer intercalations including van der Waals force or electrostatic attraction through oppositely charged species between two layers. Metal dichalcogenides, metal oxyhalides, metal phosphorous trisulphides, metal oxides, metal phosphates, hydrogen phosphates, phosphonates, graphite and layered clay minerals usually serve as host lattices; on the other hand, metal ions, organic molecules and organometallic molecules can be used as guest materials. The incorporation of guest species brings various structural changes to host lattices. The

principle geometrical transitions of layered host lattice matrices upon intercalation of guest species include: (1) change in interlayer spacing; (2) change in the stacking mode of the layers; (3) formation of intermediate phases at low guest concentrations that may exhibit staging [7]. A variety of synthesis methods have been developed for the formation of intercalation compounds [5,8]. The direct reaction of the guest species with the host lattice is the simplest and most commonly used method, and in which the intercalation reagent must be good reducing agents of the host crystals [9]. A guest ion in an intercalation compound can be replaced with another guest ion by ion exchange, which offers a useful route for intercalating large ions that do not directly intercalate [10]. The ion exchange reactions are facilitated by flocculating and reflocculating the host structure as long as appropriate solvents or electrolytes are chosen [11]. Another important method to prepare intercalation compounds is electrointercalation in which the host lattice serves as the cathode of an electrochemical cell [12]. For example, the formation of vanadium bronzes can be achieved by electrochemical lithium intercalation together with compensating electrons as follows:

$$V_2O_5 + xLi^+ + xe^- \Leftrightarrow Li_xV_2O_5 \qquad (1)$$

Figure 1.1 shows the principal concept of Li-ion batteries. It typically consists of a negative lithium intercalation material (anode) and another lithium intercalation material with a more positive redox potential (cathode). The anode and cathode are separated by the electrolyte. The electrolyte must be an electronic insulator but a Li-ion conductor.

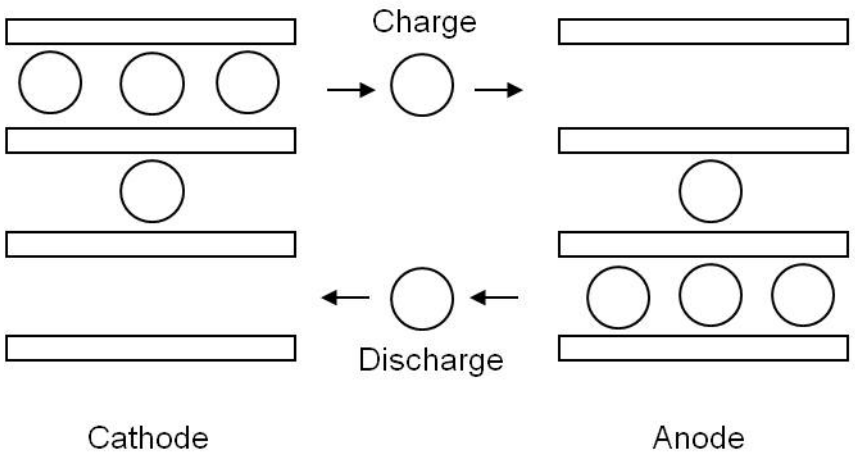

Figure 1.1 Schematic illustration of a Li-ion battery.

Lithium ions are extracted from the cathode and inserted into the anode when the battery is charged. This process takes place reversely when the battery is discharged. Metallic lithium was used as the anode in early batteries due to its very negative redox potential and low weight. It was later replaced by carbon because of safety concerns. Both cell life and safety are improved with the replacement of the metallic lithium or carbon by lithium intercalation compounds. Three fundamental requirements must be fulfilled for electrode materials to reach the goal of a high specific energy: (1) a high specific charge and discharge density, i.e., a high number of available charge carriers per mass and volume unit of the material; (2) a high cell voltage, resulting from a high (cathode) and low (anode) standard redox potential of the respective electrode redox reaction; and (3) a high reversibility of electrochemical reactions at both cathodes and anodes to maintain the specific charge for hundreds of charge/discharge cycles. Numerous lithium intercalation electrodes have been proposed for a rechargeable lithium cell since the early 1970s. This thesis focuses on the cathode materials, which are much less developed than anodes [13].

1.3 Typical Cathode Materials

There are two categories of cathode materials. Layered compounds such as $LiTiS_2$, $LiCoO_2$, $LiNi_{1-x}Co_xO_2$, and $LiNi_x Mn_xCo_{1-2x}O_2$ belong to one group. They have anion close-packed lattice; transition metal cations occupy alternate the layers, and remaining empty layers are occupied by lithium ions. The spinels with the transition metal cations ordered in all the layers are also considered to be in this group. The other group of cathode materials has more open structures, such as vanadium oxides, tunnel compounds of manganese oxides, and transition metal phosphates (e.g., the olivine $LiFePO_4$). This group of materials generally provides better safety and lower cost.

1.3.1 Vanadium Pentoxide

Vanadium pentoxide (V_2O_5) is a typical intercalation compound because of its layered structure. As shown in Figure 1.2, orthorhombic crystalline V_2O_5 consists of layers of VO_5 square pyramids that share edges and corners [14-15]. Low cost, abundant source, easy synthesis, and high energy densities are essential advantages of V_2O_5 for Li-ion intercalation applications. Whittingham first reported the reversible electrochemical lithium intercalation into V_2O_5 at room temperature in 1975 [16].V_2O_5 exhibits several phases when different amounts of lithium are inserted. $Li_xV_2O_5$ shows α-phase and ε-phases for $x < 0.01$ and $0.35 < x < 0.7$, respectively. These two phases show a similar structure with V_2O_5 in spite of increasing puckering of the layers [17].

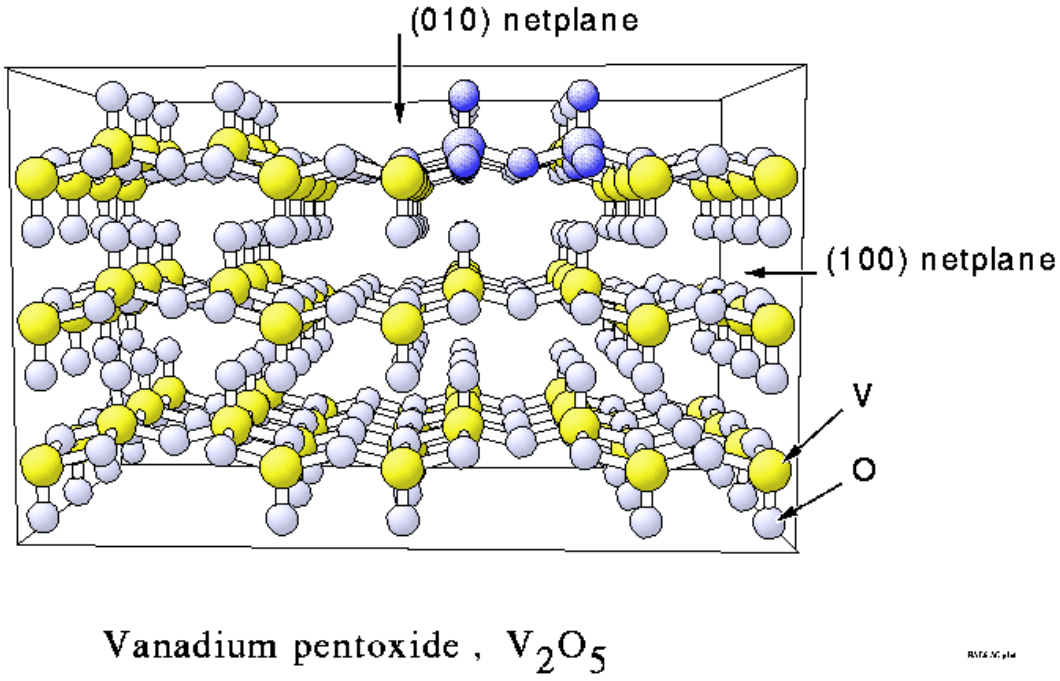

Figure 1.2 Crystal structure of V_2O_5 (http://www.fhi-berlin.mpg.de/~hermann/Balsac/BalsacPictures/V2O5bulk.gif).

For x=1, LiV_2O_5 shows δ-phase which forms by the gliding of one layer out of two [18]. For $x \leq 1$, the original V_2O_5 structure can be recovered upon lithium deintercalation, and the phase transitions are fully reversible [19]. However, for further lithium intercalation ($x > 1$), δ-phase transforms to γ-phase dominated by a reconstruction mechanism, and this transformation is not reversible **[**17]**.** The γ-type structure of $Li_xV_2O_5$ can be maintained with the stoichiometric range $0 < x < 2$ [20-21]. Upon further intercalation of a third lithium, ω-phase with a rock-salt type structure substitutes the γ phase, and this transformation is also irreversibe. This ω-phase can be prepared either electrochemically at a potential of about 1.2 V vs. Li/Li^+ or chemically using an excess of butyl lithium [22-23]. Almost all the lithium from the ω-phase can be electrochemically deintercalated again. A specific energy of up to 900 Wh/kg is demonstrated by the resulting compound, and the specific energy

maintains more than 450 Wh/kg after 100 cycles in a voltage range between 3.4 V and 1.9 V. Therefore, ω-$Li_xV_2O_5$ showed great potential as positive electrode material for secondary lithium batteries [24]. Hydrated vanadium pentoxide ($V_2O_5 \cdot nH_2O$) such as $V_2O_5 \cdot nH_2O$ xerogels [25,26] and $V_2O_5 \cdot nH_2O$ aerogels [27] can also deliver high Li intercalation capacity. Li-ion cells with a xerogel cathode demonstrate specific energies of over 700 Wh/kg [26]. However, crystalline V_2O_5 suffers from low Li-ion diffusion coefficient (10^{-12} cm^2/s) and the electronic conductivity ($10^{-2} \sim 10^{-3}$ S/cm) and cannot sustain a large specific capacity at high charge/discharge rates [28-30]. Many studies have been conducted to improve Li-ion diffusion and electronic conduction in V_2O_5 by synthesizing the oxide with a more open crystal structure [31-33] or by incorporating highly conductive materials into V_2O_5 [34-36].

1.3.2 Lithium Cobalt Oxide

Lithium cobalt oxide ($LiCoO_2$) belongs to the first group of cathode materials and is the most popular for Li-ion batteries owing to the high energy density, relatively stable cycling performance and simplicity of preparation. Both solid-state and wet chemical approaches can synthesize $LiCoO_2$ conveniently [37-39]. The Li_xCoO_2 exhibits excellent cyclability at room temperature for $0.5 < x < 1$. However, the capacity retention decreases seriously when more Li is deintercalated from Li_xCoO_2 ($x < 0.5$) [40]. There are two reasons for the capacity fading of $LiCoO_2$. The first concern is the oxidization of Co^{3+}. As lithium is extracted from $LiCoO_2$, Co^{3+} is oxidized to unstable Co^{4+} during the charge process. The cathode crystallinity deteriorates with high concentration of Co^{4+}, and the c-axis dimension decreases

because of this phase transition. The second concern is the dissolution of Co^{3+}. $LiCoO_2$ decomposes in the electrolyte solution, which directly reduces the amount of effective cathode material, and thus leads to significant capacity degradation [41,42]. In order to improve the structural stability of $LiCoO_2$, coatings of carbon or various oxides such as Al_2O_3 [40] and ZnO [43] have been studied and significant improvements in capacity retention have been demonstrated.

1.4 Atomic Layer Deposition Techniques

Most surface modifications of cathode materials reported in literature are carried out with wet chemical methods [44-46], such as soaking cathode materials into 2-propanol containing aluminum tri 2-propoxide followed by heat treatment [46]. These wet methods are not well-controlled processes. The resulting coatings lack conformality, uniformity, and completeness. There is no precise control of thickness or weight ratio to the cathode materials, limiting the repeatability and reliability of these processes. As discussed in section 1.3.2, the capacity retention of $LiCoO_2$ can be enhanced by surfacing coating of various oxides such as Al_2O_3 and ZnO. The improvement of the coated $LiCoO_2$ significantly depends on the property of the coatings such as coverage rate and thickness [47-48]. Therefore, it is very important to utilize a deposition technique which can control the properties of coating conveniently and precisely.

Atomic layer deposition (ALD) was developed in the 1970s as a method to grow thin electroluminescent films on large and non-planar substrates [49]. ALD began to attract considerable attention in the following decades due to its ability to grow

ultrathin and highly-conformal layers with atomic-scale thickness and composition control [50-52]. The fundamental advantage of ALD is that the film growth is surface-controlled, rather than source-controlled as in chemical vapor deposition (CVD) or molecular beam epitaxy (MBE). This is achieved by using sequential exposures, separating the (usually binary) reaction between the precursor compounds into two half-reactions. During each half reaction only one monolayer of the reactant chemisorbs (or is chemically bound) on the surface. If the substrate temperature is kept sufficiently high, further layers which are only physisorbed are removed by a inert purge gas purge before the other reactant is introduced. As a result, the process proceeds step-wise in self-limiting surface reactions, separated by purge steps. Each full reaction cycle leads to the formation of one monolayer. Therefore, films grown using ALD are typically uniform, dense, homogenous, pinhole-free, and extremely conformal to the underlying substrate. composite films [53], as shown in Figure 1.3.

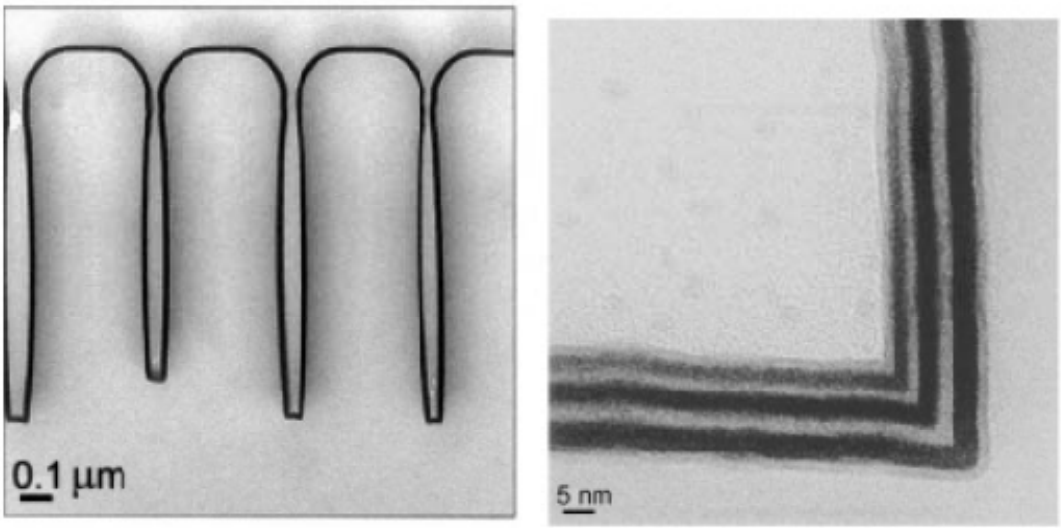

Figure 1.3 TEM images of $Hf_xAl_yO_2$ composite structure. Right image is detail of bottom corner [53].

Moreover, the film thickness is conveniently controlled by the number of reaction cycles and the growth rate mainly depends on the length of each exposure/purge cycle. Therefore, ALD is unique in the sense that it allows for the growth of conformal films even on substrates with complex surface geometries. It has been used to infiltrate pores of anodized alumina membranes [54] and deposit high-aspect ratio multilayer.

Figure 1.4 shows the process of growing ZnO film with the ALD method. The two precursors, H_2O and $Zn(CH_2CH_3)_2$ (DEtZn), are introduced separately into the reactor, and the ZnO grows layer by layer. ALD growth of ZnO is based on the binary chemical vapor deposition reaction between DEtZn and water:

$$Zn(CH_2CH_3)_2 + H_2O \rightarrow ZnO + 2\,C_2H_6 \qquad (2)$$

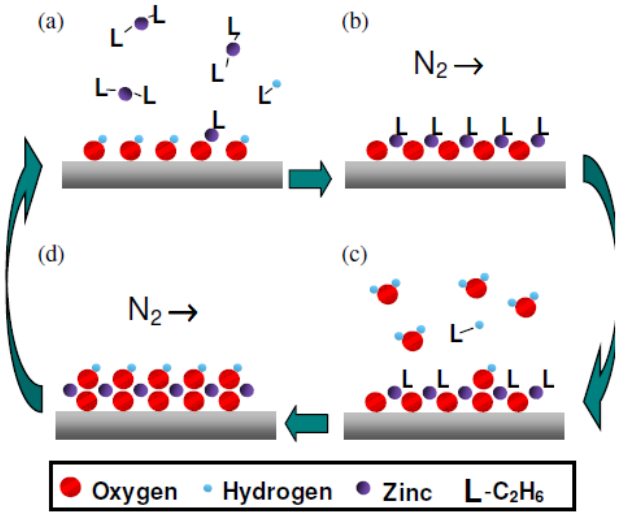

Figure 1.4 Schematic showing atomic layer deposition of ZnO [55]. Precursors are introduced separately into a viscous-flow reactor, limiting growth rate to one monolayer per cycle. ZnO grows layer-by-layer.

ALD growth is supposed to occur by splitting this reaction into the separate surface reactions:

$$ZnOH^* + Zn(CH_2CH_3)_2 \rightarrow ZnO\text{-}ZnCH_2CH_3^* + C_2H_6 \qquad (3)$$

$ZnCH_2CH_3$* +H_2O → ZnOH* + C_2H_6 (4)

where * denotes a surface species. Due to the reactivity of the organometallic precursor, this process can be operated at a temperature as low as 80ºC.

Figure 1.5 shows a typical gas pulse sequence used for ZnO ALD: Alternating exposures to the reactants in an ABAB… sequence leads to the layer-by-layer growth of ZnO as illustrated in Figure 1.4. In a similar manner, Al_2O_3 will be deposited with atomic layer control using alternating exposures of $Al(CH_3)_3$ and H_2O, respectively.

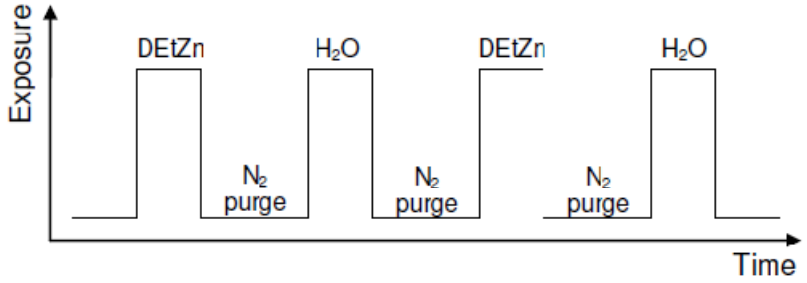

Figure 1.5 Typical pulse sequence for one ALD reaction cycle [55].

Figure 1.6 shows the schematic of an ALD system. The equipment consists of an inert carrier gas (N_2) source, a hot-wall reaction chamber, a computer-controlled gas manifold, and a mechanical pump.

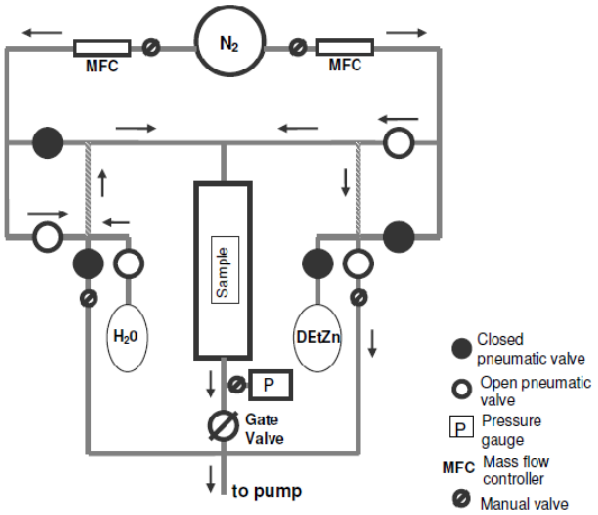

Figure 1.6 Schematic view of the ALD apparatus showing the direction of gas flow (indicated by arrows) during a water exposure [55].

During the exposure, one high-vapor pressure precursor is leaked into the gas line and transported into the chamber by the carrier gas flow. At the same time, the other precursor is purged from the system. The shaded areas indicate the parts of the manifold where gas flow reverses direction during exposure to avoid mixing of the precursors in the chamber.

1.5 Project Objectives

In sum, there are two objectives in this project. The first objective is to investigate the Li-ion intercalation properties of the solution processing of V_2O_5-WO_3 composite films. V_2O_5-WO_3 composite films with different V_2O_5/WO_3 molar ratios are prepared in order to optimize the Li-ion intercalation property. Moreover, the effects of the crystallinity and microstructure of V_2O_5-WO_3 composite films on their intercalation properties are examined with the help of XRD and SEM. The second objective of this project is to investigate the cycling performance of $LiCoO_2$ electrodes with nanosized thin coatings by ALD for Li-ion batteries. The capacity retentions of a bare $LiCoO_2$ electrode and $LiCoO_2$ electrodes with nanosized thin Al_2O_3 or ZnO coatings are compared in order to investigate the influence of the ultrathin conformal coatings by ALD.

1.6 Thesis Overview

Chapter 1 introduces Li-ion batteries and their typical cathode materials, including V_2O_5 and $LiCoO_2$. The mechanism of atomic layer deposition (ALD) is also introduced in this chapter.

Chapter 2 provides a review of the literature on V_2O_5-based composite materials

and $LiCoO_2$ with nanosized thin surface coating for Li-ion batteries.

Chapter 3 describes the solution processing of V_2O_5-WO_3 composite films for enhanced Li-ion intercalation properties. Previous work on V_2O_5-WO_3 composite films is introduced first, and then the preparation of V_2O_5-WO_3 composite films is described. The crytallinity and morphologies of the composite film are examined by XRD and SEM. The electrochemical behaviors of the composite films are investigated with the help of cyclic voltammetric measurements and chronopotentiometric measurements. Finally, the cycling performances of the composite films are compared.

Chapter 4 describes the work on the surface coating of $LiCoO_2$ by ALD for Li-ion batteries. The motivation for surface coating on $LiCoO_2$ by ALD is introduced first. The preparation of $LiCoO_2$ powders and ALD coating processes on $LiCoO_2$ are provided subsequently. The crystal structure and morphology of $LiCoO_2$ powders are investigated by XRD and SEM, respectively. The cycling performance of bare, Al_2O_3-coated and ZnO-coated $LiCoO_2$ electrodes are compared, and the mechanism for enhanced Li-ion capacity retention of Al_2O_3-coated $LiCoO_2$ electrode is discussed.

Chapter 5 summarizes the major conclusions on the solution processing of V_2O_5-WO_3 composite films and the surface coating of $LiCoO_2$ by ALD.

Chapter 2 Literature Review

2.1 Vanadium Pentoxide-Based Composite Materials for Li-Ion Batteries

As noted above, the Li-ion intercalation property of V_2O_5 is limited due to the poor electronic conductivity. The electrochemical kinetics of V_2O_5 can be improved by embedding the oxide within an electronically conducting network. Some thin coating of conductive material can serve as the conducting network, but the coating must be within nanoscale so that ions can penetrate through and appreciable polarization will not occur. Some surface modifications not only alleviate the problem of low electronic conductivity, but also reduce the size of active material, which would shorten the diffusion length for lithium.

2.1.1 Carbon-Vanadium Pentoxide Composite

Carbon-vanadium oxide composite is one of the commonly studied V_2O_5-based composites. Burning off carbon-coated V_2O_3 nanoparticles around 400ºC in air is one method to prepare carbon-coated V_2O_5 nanoparticles [56]. Varying the conditions of the burning process can manipulate the thickness and weight percentage of carbon; the optimal carbon content is found to be 2-3% by weight. These V_2O_5-C nanoparticles have good interparticle electrical contact, and do not have the usual drawbacks of nanoparticles such as poor active mass integrity and high surface reactivity. Therefore, higher capacity, better rate capability and cyclability are exhibited by carbon-coated V_2O_5 nanoparticles compared with V_2O_5 microparticles or nanoparticles. The V_2O_5-C nanoparticles can deliver a Li intercalation capacity of 290 mAh/g at high rates. Vanadium oxide/carbon nanotube nanocomposite is another

carbon-vanadium oxide composite and it can deliver higher capacities. A sol-gel method was used by Dunn's group to incorporate V_2O_5 aerogels into single-wall carbon nanotubes [57]. Intimate contact in the nanoscale between the carbon nanotubes and V_2O_5 is found, which is ascribed to the similar morphology and dimensional scale of the carbon nanotubes and V_2O_5 nanoribbons in the aerogel. Moreover, electrolyte can access throughout the composite material due to the porous structure of carbon nanotubes and V_2O_5 aerogel permits. As a result, high capacities exceeding 400 mAh/g are achieved by such nanocomposite electrode at high rates. Another method to prepare V_2O_5-C composite is by drying the precursor which contains V_2O_5 sol, carbon and a surfactant as reported by Akira Kuwahara et al. [58]. The authors claim that this V_2O_5-C composite has a short lithium diffusion distance (< 13 nm) and high electric conductivity (> 3.4 S/cm), and thus good electrochemical performance at a high discharge rate (30 A/g) is achieved. In addition, V_2O_5 xerogel-carbon composite can be prepared by starting from the solution of V_2O_5 in hydrogen peroxide and then adding 10 wt.% of carbon black into the solution [59]. The electrochemical performance of this composite was tested in saturated aqueous solutions of $LiNO_3$ and has a relatively high capacity of 123 mA·h/g compared to pure V_2O_5.

2.1.2 Polymer-Vanadium Pentoxide Composite

Conductive polymer/transition metal oxide composites have attracted much interest over the past two decades. Conductive organic polymers (e.g. polyacetylene, polyaniline and polypyrrole (PPy), pyridinesulfonic acid (PSA)) are interleaved

between the layers of an oxide lattice such as V_2O_5 in the hybrid material. The polymer/oxide composites are very attractive as the cathode material for lithium batteries, because both oxide and polymer are electrochemically active. A chemical polymerization process is utilized to prepare a PSA-PPy-V_2O_5 composite [60]. The hybrid material is more homogenous due to the addition of PSA which increases the spacing between the oxides, and this hybrid material exhibits better electrochemical characteristics. V_2O_5 nanocomposites alternating with polymer layers can be synthesized using a layer-by-layer (LbL) technique based on physical adsorption of oppositely charged layers. For example, the LbL technique is used to fabricate V_2O_5/polyaniline nanocomposite film, and the intercalation capacity is enhanced due to the intimate contact between the oxide and polymer within nanoscale [61]. Another example for the LbL technique is preparing V_2O_5 nanocomposite alternating with blends of chitosan and poly(ethylene oxide) (PEO), and the charge storage capability in such nanoarchitectures is investigated [62]. The adsorption of alternate layers of PEO and V_2O_5 is not efficient, but it can be improved by adding a small amount of chitosan (1%) into PEO. The V_2O_5/blend can intercalate 1.77 moles of lithium per mole of V_2O_5, and thus a higher capacity is achieved. The V_2O_5/blend has a larger number of electrochemically active sites, and faster lithium diffusion occurs within the host material, yielding an enhanced electrochemical performance in comparison with V_2O_5/chitosan. At 20 mV/s, the charges injected were 3.29 mC/cm^2 and 8.02 mC/cm^2 for V_2O_5/chitosan and V_2O_5/blend, respectively.

Recently Ponzio et al. reported that V_2O_5/polyaniline nanocomposite with

homogeneous distribution of polyaniline can stabilize the capacity [63]. The V_2O_5/polyaniline nanofibers are prepared using a reverse micelle method, and the composite nanofibers exhibit improved cycling performance compared to the V_2O_5 nanofibers [63]. A steady capacity of ~300 mAh/g is delivered by the V_2O_5/polyaniline nanofibers containing 30 mol% polyaniline, and the morphology does not change over 10 cycles, whereas the V_2O_5 nanofibers do not retain the morphology after cycling. Some V_2O_5/polymer nanocomposites show lower storage capacity but better cycling stability compared to pure nanostructured V_2O_5 [64]. Reddy et al. reported a hydrothermal method to prepare $PVP_xV_2O_5$ (x = 0.5, 1) nanobelts which exhibit lower capacity but better cycleability compared with V_2O_5 nanobelts. The interaction between the oxide and polymer is studied with Fourier transformation infrared spectroscopy (FTIR). It is found that the electrostatic interaction between the V_2O_5 interlayer and lithium ions is effectively shielded by the hydrogen bonds between the hydrogen atoms in PVP and the oxygen atoms of the V=O bonds of V_2O_5 nanobelts.

2.1.3 Metal-Vanadium Pentoxide Composite

Another popular composite cathode is metal-based cathode material, exemplified by the Ni-$V_2O_5 \cdot nH_2O$ core-shell structure. A two-step electrodeposition method has been used to prepare Ni-$V_2O_5 \cdot nH_2O$ core-shell nanocable arrays [65]. In the first step, a template-based electrochemical deposition was used to grow Ni nanorod arrays; in the second step, a sol electrophoretic deposition was utilized to deposit a hydrated vanadium pentoxide shell onto the surface of nickel nanorods.

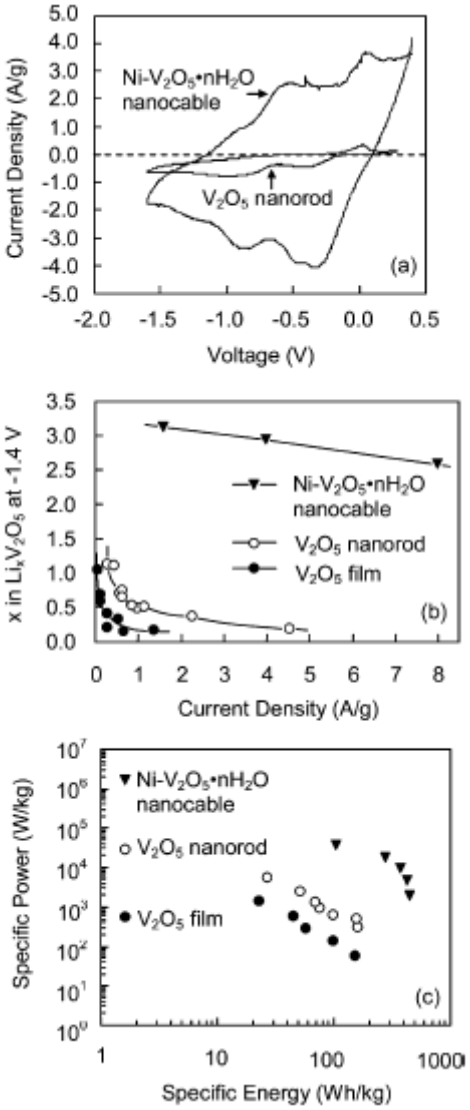

Figure 2.1 (a) Cyclic voltammograms of Ni-V_2O_5·nH_2O nanocable array and V_2O_5 nanorod array using a scan rate of 10 mV/s. (b) Relationship between current density and Li intercalation capacity of Ni-V_2O_5·nH_2O nanocable array, V_2O_5 nanorod array and sol-gel film from chronopotentiometric measurements. (c) Ragone plot for Ni-V_2O_5·nH_2O nanocable array, V_2O_5 nanorod array and sol-gel film [65].

The electrochemical performances of Ni-V_2O_5·*n*H_2O nanocable arrays, single-crystal V_2O_5 nanorod arrays and sol-gel derived V_2O_5 films are compared as shown in figure 2.1. Remarkably improved capacity and rate capability are exhibited in Ni-V_2O_5·*n*H_2O nanocable arrays compared with the other two. As the current density (discharge rate) increases, the intercalation capacities of both nanorod arrays and sol-gel films decrease rapidly. In constrast, nanocable arrays are able to

retain the high capacity as shown in Figure 2.2(b), indicating the excellent high-rate performance of nanocable arrays. Ni-$V_2O_5 \cdot nH_2O$ nanocable arrays have enhanced surface area and reduced internal resistance; thus they have significantly higher energy density and power density than those of the nanorod array and sol-gel film by at least one order of magnitude as shown in Figure 2.1(c).

Apart from Ni-$V_2O_5 \cdot nH_2O$ composite, Wang et al. synthesized Ag-$Ag_{0.08}V_2O_5 \cdot nH_2O$ composite films by dispersing silver nanowires into a $V_2O_5 \cdot nH_2O$ matrix [66]. Further amorphization of $V_2O_5 \cdot nH_2O$ is found in the composite film, and the composite film is more porous and electronically conductive. As a result, twice the capacity of the $V_2O_5 \cdot nH_2O$ xerogel film is delivered by the composite film.

2.1.4 Oxide-Vanadium Pentoxide Composite

In addition to the metal-V_2O_5 composite, oxide-V_2O_5 composites especially for TiO_2-V_2O_5 composites have attracted extended interest. The improvement of cycling performance by incorporating V_2O_5 with TiO_2 has been reported by several groups [67-69]. However, TiO_2-V_2O_5 composite exhibits different behavior on Li-ion intercalation capacities. M.B. Sahana et al. reported that the lithium intercalation capacity of a TiO_2-V_2O_5 composite decreases from 47 mC/cm^2 to 27 mC/cm^2 with incorporation of 5% Ti if titanium (IV) 2-ethylhexoxide and vanadium naphthenate oxide are utilized as metalorganic precursors. On the other hand, the capacity of a TiO_2-V_2O_5 composite increases from 14 mC/cm^2 to 27 mC/cm^2 using vanadium-tri(isopropoxide) oxide [$VO(OC_3H_7)_3$] and titanium(IV) tetra-isopropoxide

as precursors [70]. Kyoungho Lee et al. claimed that the fabrication method, morphology, and crystallinity significantly influence the electrochemical performances of TiO_2-V_2O_5 composites, and the Li-ion intercalation capacity is considerably enhanced by dropping the mixture of V_2O_5 sol and $TiOSO_4$ solution on Ti substrate and drying it under ambient conditions [71]. For example, the TiO_2-V_2O_5 composite with a V/Ti molar ratio of 80/20 delivers a discharge capacity of ~425 mAh/g at a current density of 0.27 A/g, which is nearly twice of that delivered by pure V_2O_5. Moreover, TiO_2-V_2O_5 composite nanorod arrays are prepared with the help of polycarbonate (PC) membranes, and enhanced intercalation capacities are exhibited by the TiO_2-V_2O_5 composite nanorod arrays with a V/Ti molar ratio of 75/25 [72].

2.2 Lithium Cobalt Oxide with Nanosized Thin Surface Coating

The lithium transition metal oxides such as $LiCoO_2$, $LiMn_2O_4$, or their solid solutions are popular cathode materials for Li-ion batteries. However, they can react with the electrolyte, which leads to safety problems. On the other hand, they can dissolve in the electrolyte as well, which deteriorates the cycling performance significantly. Coating the electrode materials with a nanosized thin surface layer is proved to enhance the stability of these lithium metal oxides.

Various MPO_4 (M = Al, Fe, SrH and Ce) coatings on $LiCoO_2$ have attracted much interest. $FePO_4$-coated $LiCoO_2$ is prepared via a co-precipitation method [73]. The anti-overcharge and thermal stability as well as the structural stability are improved by the $FePO_4$ coating. The effect of the MPO_4 nanoparticle coatings on $LiCoO_2$

were studied extensively by Kim et al. [74]. It is found that with the coating concentration and annealing temperature, the nanoparticle size and morphology affect the extent of the coating coverage. $LiCoO_2$ is fully encapsulated by smaller nanoparticles of $AlPO_4$ or $FePO_4$ with a size less than 20 nm, whereas $LiCoO_2$ is only partially covered by $CePO_4$ particles with a size larger than 150 nm or whisker-shaped $SrHPO_4$. The highest intercalation capacity of 230 mAh/g is delivered by the $LiCoO_2$ fully covered by $AlPO_4$ or $FePO_4$ in a voltage range of 4.8 and 3 V at a rate of 0.1 *C*. The best capacity retention is shown by the $AlPO_4$-coated $LiCoO_2$; the $FePO_4$-coated cathode shows lower capacity retention than the $CePO_4$- and $SrHPO_4$-coated cathodes at 90ºC, which is attributed to the continuous Fe metal ion dissolution at this temperature. In spite of the differences of the coated $LiCoO_2$ cathodes, the coatings suppress cobalt dissolution, and thus electrochemical performances are improved. In a further investigation of $AlPO_4$-coated $LiCoO_2$, electrochemical properties of $AlPO_4$-nanoparticle-coated $LiCoO_2$ at various cutoff-voltages were found to depend on the annealing temperature [75]. The $AlPO_4$-coated cathodes exhibit excellent electrochemical performance with high cutoff voltages larger than 4.6 V when annealed at 600 ºC and 700 ºC, while such cathodes annealed at 400ºC show a lower capacity and poorer rate capability. However, optimal capacity retention is shown by the $AlPO_4$-coated $LiCoO_2$ annealed at 400ºC [76]. Typical TEM images of $AlPO_4$-coated $LiCoO_2$ deposited at room temperature, 400ºC and 700ºC are shown in figure 2.2.

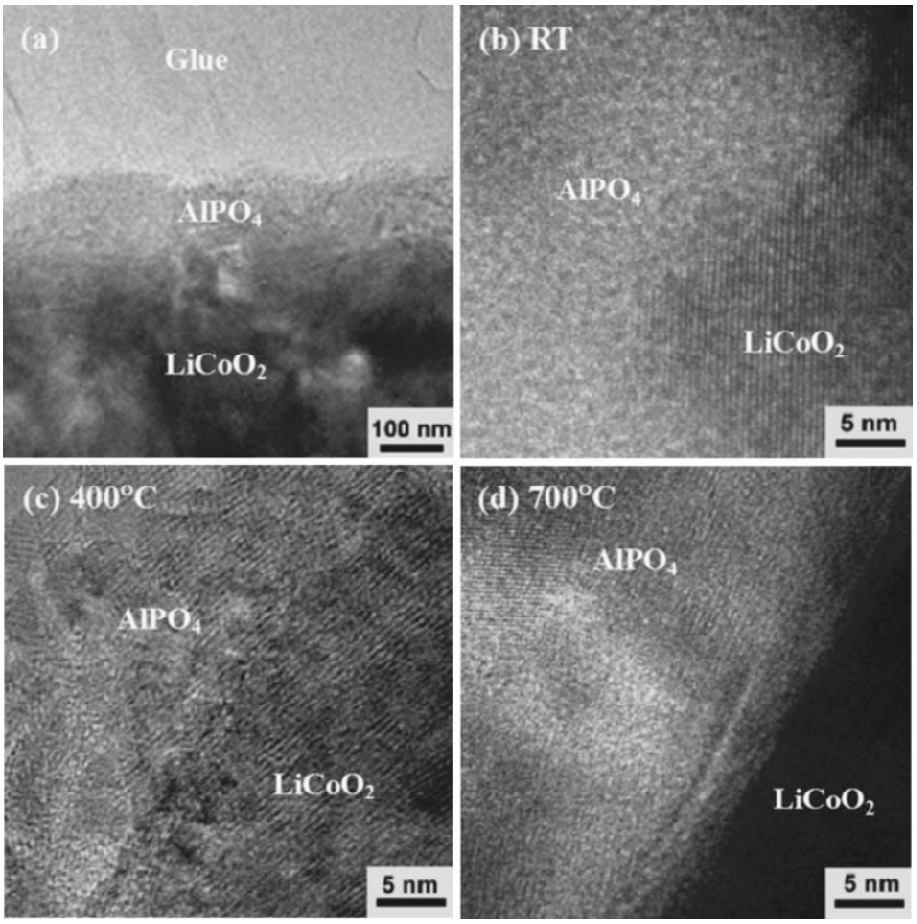

Figure 2.2 (a) Cross-sectional TEM images of $AlPO_4$-coated $LiCoO_2$. A ~100 nm thick $AlPO_4$ continuous layer is coated on the $LiCoO_2$. High resolution images of the AlPO4-coated $LiCoO_2$ at (b) room temperature, (c) 400ºC, and (d) 700ºC [76].

A continuous layer of $AlPO_4$ coated on the surface of $LiCoO_2$ has a thickness of about 100 nm as shown in Figure 2(a). Figure 2(b) shows that the coating layer deposited at room temperature is amorphous. Figure 2(c) shows that the nanocrystals in coating deposited at 400ºC have a size range of 3-5 nm, and the coating deposited at 700ºC consists of ~20-30 nm in size as shown in figure 2(d). The nanostructures of the coating layer and the interdiffusion at the interface between the coating layer and the $LiCoO_2$ cathode change with different annealing temperatures, which explains the effect of temperature on electrochemical properties of $AlPO_4$-coated $LiCoO_2$.

In addition to coatings of phosphates, surface modification of $LiCoO_2$ by coating various oxides such as ZrO_2 [77], Al_2O_3 [78], SnO_2 [79], MgO [80] or ZnO [43] has been widely investigated. In the case of ZnO-coated $LiCoO_2$, the cobalt dissolution is reduced due to the ZnO coating which also prevents the inorganic surface films such as LiF from covering the $LiCoO_2$ particles [43]. Based on the impedance spectra, the ZnO coating layer can also reduce the charge-transfer resistance of the coated $LiCoO_2$, although the ZnO coating layer is more resistant than the $LiCoO_2$ surfaces. As a result, the high-voltage cycleability of the $LiCoO_2$ cathodes is improved by surface modification with ZnO. In addition to the ZnO coating, the $LiCoO_2$ cathode surface can be protected and the electrolyte decomposition can be reduced at high voltages by coating ZrO_2 on $LiCoO_2$ [81-82]. Improved structural stability is exhibited by the ZrO_2-coated $LiCoO_2$ compared to the bare $LiCoO_2$, as evidenced by in situ XRD data. Moreover, $LiCoO_2$ coated with different weight percents of $3LaAlO_3$:Al_2O_3 was reported by Cheng-Zhang Lu et al. [83]. The electrical conductivity can be enhanced by $LaAlO_3$ and PF_6^-, PF_5, and HF in the electrolyte can be collected by amorphous Al_2O_3. The best electrochemical performance is exhibited by the $3LaAlO_3$:Al_2O_3-coated $LiCoO_2$ with 1.0 wt% $3LaAlO_3$:Al_2O_3, which delivers a discharge capacity of 138 mAh/g after 182 cycles. This discharge capacity is larger than that delivered by pristine $LiCoO_2$ after 38 cycles.

Chapter 3 Solution Processing of V_2O_5-WO_3 Composite Films for Enhanced Li-Ion Intercalation Properties

3.1 Introduction to V_2O_5-WO_3 Composite Films

Intercalation compounds as a special family of materials have attracted tremendous research interests recently. The intercalation refers to the reversible intercalation of mobile guest species (atoms, molecules, or ions) into a crystalline host lattice that contains an interconnected system of an empty lattice site of appropriate size, while the structural integrity of the host lattice is formally conserved. Various host lattices are metal dichalcogenides, metal oxyhalides, metal phosphorus trisulfides, metal oxides, metal phosphates, hydrogen phosphates, phosphonates, graphite and layered clay minerals. Guest materials include metal ions, organic molecules, and organometallic molecules. In particular, Li-ion intercalation compounds have received extensive attention due to their applications as electrode materials in Li-ion rechargeable batteries [84-90], electrochemical supercapacitors [91-92], and electrochromic devices [93-95]. Among various transition metal oxides that are capable of intercalating Li ions, vanadium pentoxide (V_2O_5) has been studied widely for several decades [96-100]. V_2O_5 can intercalate Li ions or other molecules due to its layered structure and has a theoretical capacity of 144 mA•h/g for one mole Li-ion intercalation per mole V_2O_5 [16,101]. The chemical energy is transformed to electric energy during intercalation and this process can be carried out reversely during deintercalation [71]. Based on this electrochemical property, V_2O_5 has become a promising electrode material for rechargeable Li-ion batteries [102-103], electrochemical supercapacitors [91-92], and electrochromic displays [93, 104-105].

However, the Li-ion diffusion coefficient (10^{-12} cm^2/s) and the electronic conductivity (10^{-2} to 10^{-3} S/cm) in crystalline V_2O_5 are inherently too low to sustain a large specific capacity at high charge/discharge rates [28-30]. Many studies have been conducted to improve Li-ion diffusion and electronic conduction in V_2O_5 by synthesizing the oxide with a more open crystal structure [31-33] or by incorporating highly conductive materials into V_2O_5 [34-36]. Recently Anqiang Pan et al. reported that the charge transport in V_2O_5 is improved by forming coherent hydrous vanadium pentoxide–carbon cryogel nanocomposites and the carbon network provides good electrical conductivity, hence the lithium interaction capacity of V_2O_5 is significantly enhanced [100].

Another approach to improve lithium interaction capacity of V_2O_5 is modifying its crystallinity by annealing V_2O_5 xerogel films at 300°C in nitrogen and air [99] or by adding other electrochemically active species such as titanium dioxide (TiO_2) [72]. In this study, we will incorporate tungsten trioxide (WO_3) into V_2O_5 via solution processing of V_2O_5-WO_3 composite films. WO_3 shows electrochromic properties due to its capability of intercalating various cations (H^+, Li^+, and K^+) and can deliver a capacity of 115 mA•h/g theoretically for one mole Li-ion intercalation per mole WO_3. Thus WO_3 has found wide applications in electrochromic displays and smart windows [94-95,106-109]. For example, Wang et al. recently reported the synthesis of uniform crystalline WO_3 nanorods by using a facile hydrothermal process; the assembly of these nanorods without any surfactants results in transparent WO_3 nanorod film, which demonstrates excellent electrochromic properties with high

stability over 1000 Li-ion intercalation/deintercalation processes [108]. The electrochromic performance of WO_3 can be further improved by forming V_2O_5-WO_3 composite materials [110]. It has been reported that the composite film with a V_2O_5/WO_3 molar ratio of 0.035:0.965 shows more neutral color and higher coloration efficiency in comparison to pure WO_3 [110]. The WO_3-V_2O_5 composite also exhibits improved catalytic activity, which facilitates its applications for ethanol partial oxidation [111] and NO decomposition [112]. M. Ranjbar et al. has found that the V_2O_5-WO_3 composite film with a V_2O_5/WO_3 molar ratio of 0.09:0.91 shows better response to hydrogen gas exposure for deeper and faster coloring [113].

V_2O_5-WO_3 composite films have been prepared by pulse laser deposition [114, 113] and sol-gel routes [115, 110-112]. The sol-gel processing methods offer facile control of the stoichiometry and structure of the films which will affect the charge/discharge capacity and reversibility of the V_2O_5-WO_3 composite films [110]. However, several limitations are also found in the sol-gel routes reported previously. For example, some sol-gel processing methods employ precursors such as sodium tungstate dehydrate (Na_2WO_4), sodium tungstate ($NaWO_3$), sodium metavanadate ($NaVO_3$) [111, 115], vanadium oxyisopropoxide, and tungsten hexachloride [112]. Impurity elements such as Na^+ or Cl^- are introduced into the synthetic procedure. N. Ozer and Lampert have employed a sol-gel method using vanadium triisopropoxide oxide ($VO(OC_3H_7)_3$) and metallic tungsten as the precursors of V_2O_5 and WO_3, respectively. This method avoids those impurity elements; however, the mixed sol obtained by N. Ozer and Lampert can only remain stable for several days [110].

Most V_2O_5-WO_3 composite films reported in literature have been studied for enhanced catalytic activity or electrochromic performances. In such composite films, WO_3 is usually the major constituent and its catalytic or electrochroimic properties are improved by the V_2O_5 addition. There are few reports on the electrochemical properties of V_2O_5-WO_3 composite films for applications in Li-ion batteries.

In short, we investigate the Li-ion intercalation properties of V_2O_5-WO_3 composite films for applications as cathode materials in Li-ion rechargeable batteries. We have utilized a simple and novel solution processing method to prepare the V_2O_5-WO_3 composite films with different molar ratios of V_2O_5 and WO_3. This solution processing method employs precursors that only contain the elements of V, W, O and H, and thus avoids introducing impurity elements such as Na into the sol as other sol-gel methods reported in literature. The resulted solution is stable and remains clear for several months. This solution-processing method also offers simple and precise control of V_2O_5/WO_3 compositions. It is found that V_2O_5-WO_3 composite films deliver higher Li-ion intercalation capacities than both pure V_2O_5 and WO_3 films, due to morphological and structural changes of one oxide caused by the other. In this systematic study, V_2O_5/WO_3 molar ratios are optimized to achieve the highest Li-ion intercalation capacity in the composite film. Furthermore, we have examined the effect of chemical composition, crystallinity, and microstructure of V_2O_5-WO_3 films on their intercalation properties.

3.2 Experimental Section

Mixed solutions with different molar ratios of V_2O_5:WO_3 (1:0, 10:1, 4:1, 1:1, 1:4 and 0:1) were synthesized by combining an aqueous vanadium pentoxide sol with a solution of tungsten oxygen ionic species. The vanadium pentoxide sol was prepared using a method reported by Fontenot et al.[116]. 0.136 g V_2O_5 powders (99.6%, Alfa Aesar) was dissolved in 2ml deionized H_2O and 0.603 ml H_2O_2 (30%, Mallinckrodt) solution. The suspension was stirred until the V_2O_5 powders totally dissolved, resulting in a clear and dark red solution. The solution was then sonicated to get a red brown gel which was dispersed into water in a molar concentration of 0.005 M, and was stirred until it was clear. The tungsten based solution was prepared using a method reported by Bouziane Yebka et al. [117]. The peroxopolytungstic acid was prepared by dissolving 1.247g H_2WO_4 (tungstic acid, Alfa Aesar) in 50ml H_2O_2 (30 wt% in water), resulting in a cloudy white dispersion. The dispersion was stirred for 24 hours at 60 ^oC until a clear colorless solution was obtained. This solution was further diluted in water to reach a molar concentration of 0.005 M. Without further adjusting the pH values (V_2O_5: 2.67 and WO_3: 2.30) of the individual sol and solution, the appropriate amounts of vanadium based sol and tungsten based solution were admixed by stirring for 10 min, giving a yellow solution. A droplet of the sol or solution was drop cast onto a ITO (tin-doped indium oxide) glass (1 inch × 1 inch) and dried under ambient conditions. The masses of all the films were kept at 6×10^{-5} g. The films were then heated at 110^oC for 8 h, followed by heating at 200 ^oC for 1 h and at 470 ^oC for 1 h with the same heating rate of 2 ^oC

/min in air. Annealing of the films at 470 ^{o}C results in crystalline phases of V_2O_5 and WO_3. Another annealing process was heating the films at 250 ^{o}C with a heating rate of 2^{o}C /min. The effect from amorphous WO_3 on the crystallinity of the composite films can be studied at this temperature.

The crystalline phases of the films with various V_2O_5/WO_3 molar ratios were analyzed by X-ray diffraction (XRD) using a Rigaku MiniFlex diffractometer with CuKα radiation operated at 30 kV and 15 mA. Scanning electron microscopy (SEM, Quantum 3D FEG) was used to examine the morphology of the pure V_2O_5 and WO_3 films and their composite films with V_2O_5:WO_3 =4:1 and 10:1 after heat treatment at 470 ^{o}C for 1 h. A three-electrode cell was used to investigate the electrochemical properties of the composite films with different molar ratios. A platinum mesh was used as counter electrode and a silver wire in a 0.1 mol/L $AgNO_3$ ethanol solution serves as reference electrode; the Ag/Ag^{+} reference electrode has been used for electrochemical measurements including electrochemical characterizations of vanadium-oxide-based electrode materials [100, 118-119]. The electrolyte was a 1 mol/L solution of lithium perchlorate (99%, Alfa Aesar) in propylene carbonate (99%, Aldrich). Cyclic voltammetric (CV) measurements were carried out between the potential limits of -1.6 and 0.4 V versus Ag/Ag^{+} using a potentiostat/galvanostat (Model 605C, CH Instrument). The CV curves were recorded after two cycles at a scan rate of 0.05 V/s. The chronopotentiometric measurements were carried out under various current densities.

3.3 Results and Discussion

Figure 3.1 shows the X-ray diffraction spectra of the V_2O_5, WO_3, and V_2O_5-WO_3 composite films on ITO substrates annealed at 470 ^oC for 1 h. The sol-gel-derived V_2O_5 film demonstrates a strong preferential orientation along [001] direction, which is in good agreement with the previous report [120]. The film derived from the tungsten based solution exhibits a monoclinic phase, as evidenced by the typical peak (020) at 2θ=23.67.

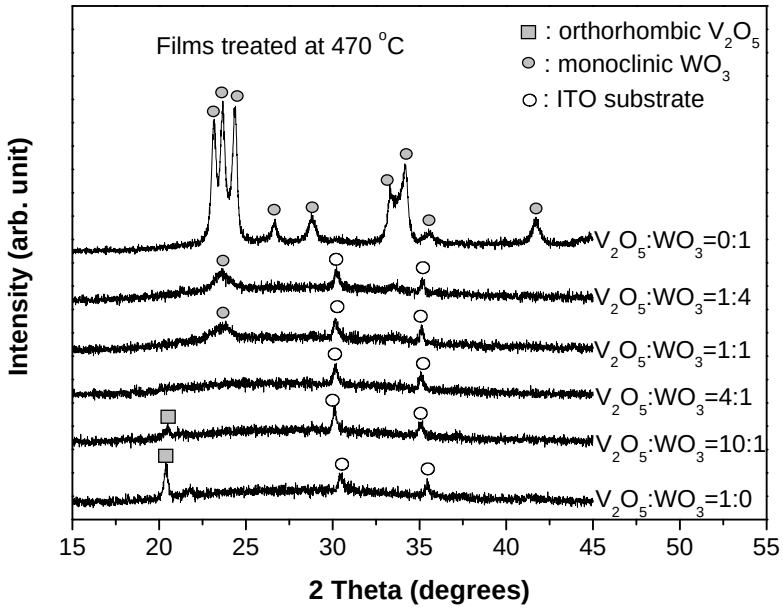

Figure 3.1 X-ray diffraction patterns of V_2O_5-WO_3 composite films after annealing at 470 ^oC in air for 1 h.

The monoclinic phase of WO_3 is also observed when the V_2O_5/WO_3 molar ratios are 0:1, 1:4 and 1:1, but its corresponding XRD peaks become weaker as more V_2O_5 emerges in the composite films. The XRD peaks of WO_3 eventually disappear with further increase in V_2O_5 and the orthorhombic phase of V_2O_5 appears when the V_2O_5/WO_3 ratio reaches 10:1. The decease of intensities of diffraction peaks indicates the deterioration of the crystallinity of oxides. As there are no new diffraction peaks other than orthorhombic V_2O_5 and monoclinic WO_3, it can be

concluded that there is no second phase. In addition, all the samples are prepared using water-based sol-gel or solution processing methods, as detailed in the experimental section; solvents (H_2O and H_2O_2) evaporate and disappear during drying and sintering, and there is no precursor loss. Thus the deterioration of the crystallinity of V_2O_5 and WO_3 is ascribed to the presence of the other oxide. It should be noted that the diffraction peaks of both WO_3 and V_2O_5 disappear when the V_2O_5/WO_3 molar ratio is 4:1, indicating possible amorphization of both oxides.

Figure 3.2 shows the XRD patterns of pure oxide and composite films treated at 250^{o}C for 5 h. Annealing at such a relatively low temperature leads to hydrated films which can be amorphous or nanocrystalline showing broad XRD diffraction peaks.

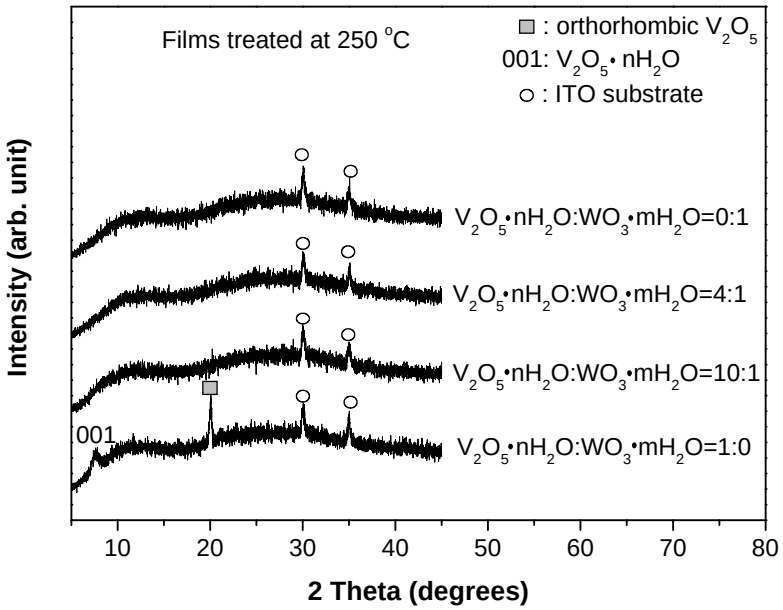

Figure 3.2 X-ray diffraction patterns of V_2O_5•nH_2O-WO_3•mH_2O composite films obtained via annealing at 250^{o}C in air for 5 h.

In the XRD patterns of pure tungsten oxide film and composite films with V_2O_5/WO_3 molar ratios of 4:1 and 10:1, no peaks related to WO_3 exist, suggesting

tungsten oxide is not crystallized yet at 250°C. In the XRD pattern of pure vanadium pentoxide film, the peak at 2θ=7.82 corresponds to the (001) diffraction of V_2O_5•nH_2O and the peak at 2θ=20.07 is ascribed to orthorhombic V_2O_5, indicating that the film annealed at 250°C contains a mixture of hydrated films and anhydrous orthorhombic phase; both peaks disappear when WO_3 is added in the composite films with V_2O_5/WO_3 ratios of 4:1 and 10:1. These results suggest that the crystallization process in the composite films is hindered with the coexistence of vanadium and tungsten ions, which occurs even at relatively low temperatures when the oxides are not fully crystallized yet.

Figure 3.3 shows the top-view SEM images of V_2O_5, WO_3, and V_2O_5-WO_3 composite films with V_2O_5/WO_3 molar ratios of 4:1 and 10:1. The V_2O_5 film is composed of platelet grains and appears dense, as shown in Figure 3.3 (a). On the other hand, the WO_3 film shows a porous structure as shown in Figure 3.3 (d), which is different from WO_3 films consisting of nanosized platelets or needle-like textured grains prepared by other solution methods reported in literature [121-122]. Figure 3.3 (b) and Figure 3.3 (c) present the surface morphology of composite films with V_2O_5/WO_3 ratios of 10:1 and 4:1, respectively. It is clear that grain sizes in these composite films are smaller than those in pure V_2O_5 films, indicating the deterioration of crystallinity. There are a small quantity of thick (diameter: ~320 nm) and thin (diameter: ~140 nm) fibers in the composite film with a V_2O_5/WO_3 molar ratio of 4:1. In the case of composite film with a V_2O_5/WO_3 molar ratio of 10:1, many nanofibers with a smaller diameter of about 70 nm exist in the film, as shown in Figure 3.3 (b).

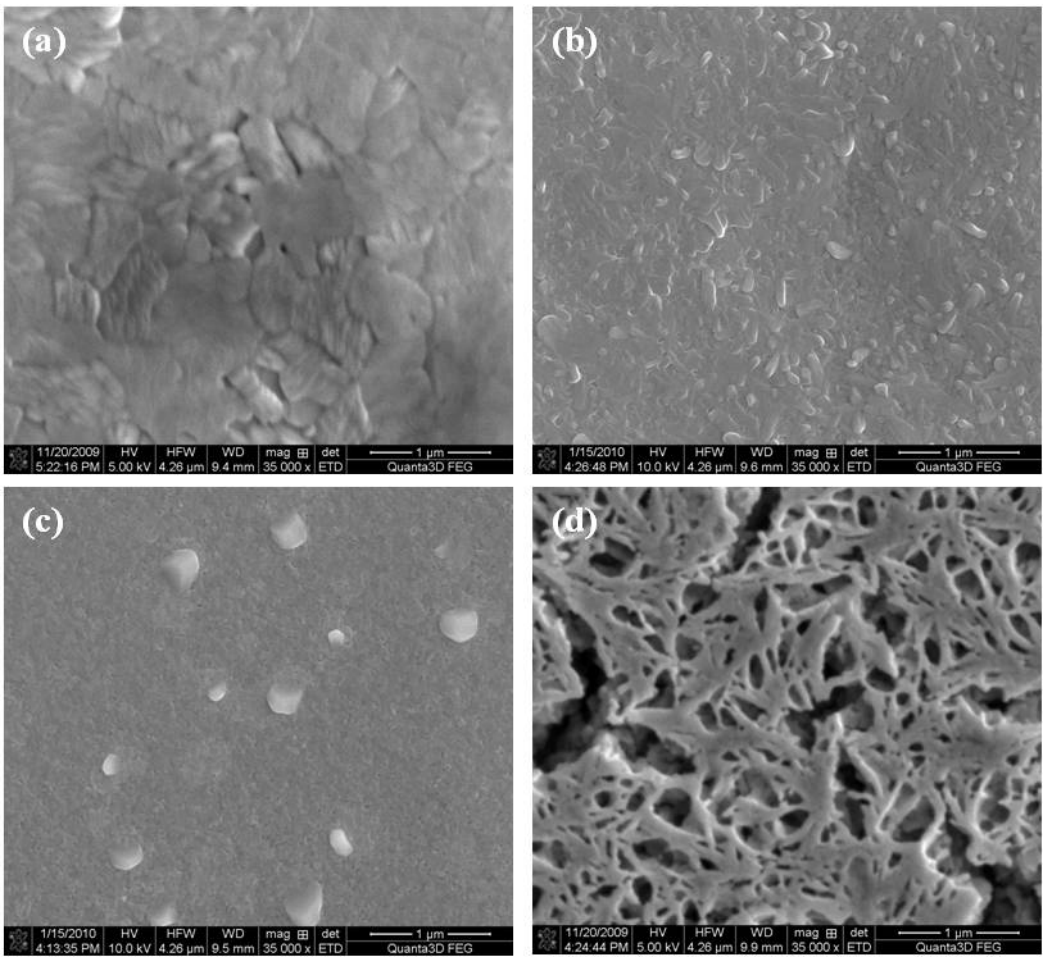

Figure 3.3 SEM micrographs showing surface morphologies of (a) pure V_2O_5 film, composite V_2O_5-WO_3 films with V_2O_5:WO_3 molar ratios of (b) 10:1 and (c) 4:1, and (d) pure WO_3 film. All the films are obtained via annealing at 470 ^oC for 1 h.

The cross-section SEM images of films with V_2O_5/WO_3 molar ratios of 1:0, 0:1, and 10:1 are presented in Figure 3.4. The cross section of pure V_2O_5 film exhibits a smooth and dense structure, with a thickness of ~215 nm. On the other hand, the cross section of WO_3 film (same mass as V_2O_5 film) shows a rough and porous granular structure and the film is much thicker (610 nm) than V_2O_5 film. Different from pure V_2O_5 film, the cross section of the composite film with a V_2O_5/WO_3 molar ratio of 10:1 shows a granular structure, although the particles are smaller than pure WO_3 film. The thickness of this composite film is ~265 nm, thicker than V_2O_5 film but thinner than WO_3 film. Since the bulk density of WO_3 (7.25 g/cm^3) is much

larger than that of V_2O_5 (3.35 g/cm^3) and all the films have the same mass, the WO_3 film with the largest thickness is the most porous and the V_2O_5 film with the lowest thickness is the least porous.

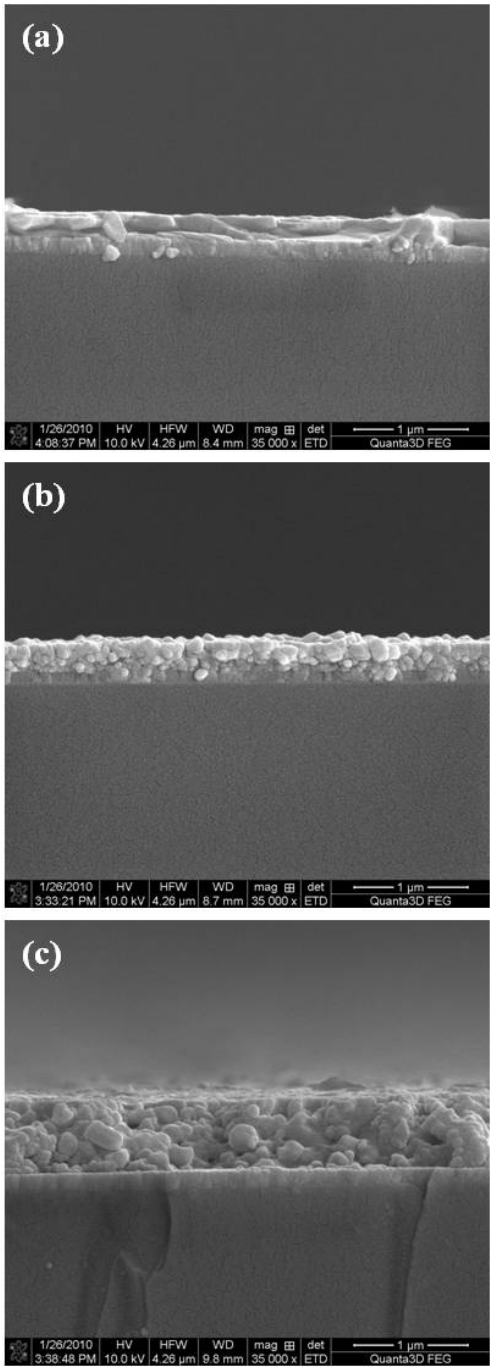

Figure 3.4 SEM micrographs showing cross-section morphologies of (a) pure V_2O_5 film, (b) composite V_2O_5-WO_3 film with a V_2O_5:WO_3 molar ratio of 10:1, and (c) pure WO_3 film. All the films are obtained via annealing at 470 ^oC for 1 h.

The V_2O_5-WO_3 composite film with the intermediate thickness is more porous than V_2O_5 film and less porous than WO_3 film. Thus the composite film has larger electrochemical active area than V_2O_5 film, which can contribute to the enhanced Li-ion intercalation property of the composite film. However, the most porous WO_3 film delivers the lowest discharge capacity despite its porous structure and large surface area. It should be noted that the capacity of WO_3 is dependent on the potential range used in electrochemical measurements. For example, according to the work of Wen-Jing Li et al. [123], WO_3 exhibits a capacity of above 800 mA·h/g in the potential range of 4.0 ~ 0.0 V vs. Li/Li^+, but the WO_3 sample exhibits much lower capacity when the potential range is reduced to 4.0 ~ 2.0 V vs. Li/Li^+. The potential range we used (0.4 ~ -1.6 V *vs*. Ag/Ag^+) is similar to the latter and thus our pure WO_3 film shows low capacity.

Figure 3.5 shows typical cyclic voltammograms (CV) of V_2O_5, WO_3 and V_2O_5-WO_3 composite films heated at 470°C measured at a scan rate of 0.05 V/s. The CV curve of WO_3 film shows indistinguishable cathodic and anodic peaks, indicating there is not much Li-ion intercalation/deintercalation within the given potential limit. On the other hand, the cyclic voltammogram of V_2O_5 film is more complicated. It shows two discernable cathodic peaks at -0.443 V, -0.735 V and three shoulders around –0.217 V, -1.179 V and -1.388 V; it shows three anodic peaks at -0.028 V, -0.547 V,-0.877 V and one shoulder around -0.240 V. The presence of cathodic and anodic peaks is attributed to Li^+ intercalation and extraction processes, respectively. The CV curve of the composite film with a V_2O_5/WO_3 molar ratios of

4:1 shows three cathodic peaks at -0.240 V, -0.438 V -0.770 V and two shoulders around -1.148 V and -1.382 V; it shows anodic peaks at -0.071 V, -0.275 V, -0.560 V, -0.794 V and one shoulder around -1.201 V. This CV curve is similar to that of the pure V_2O_5 film.

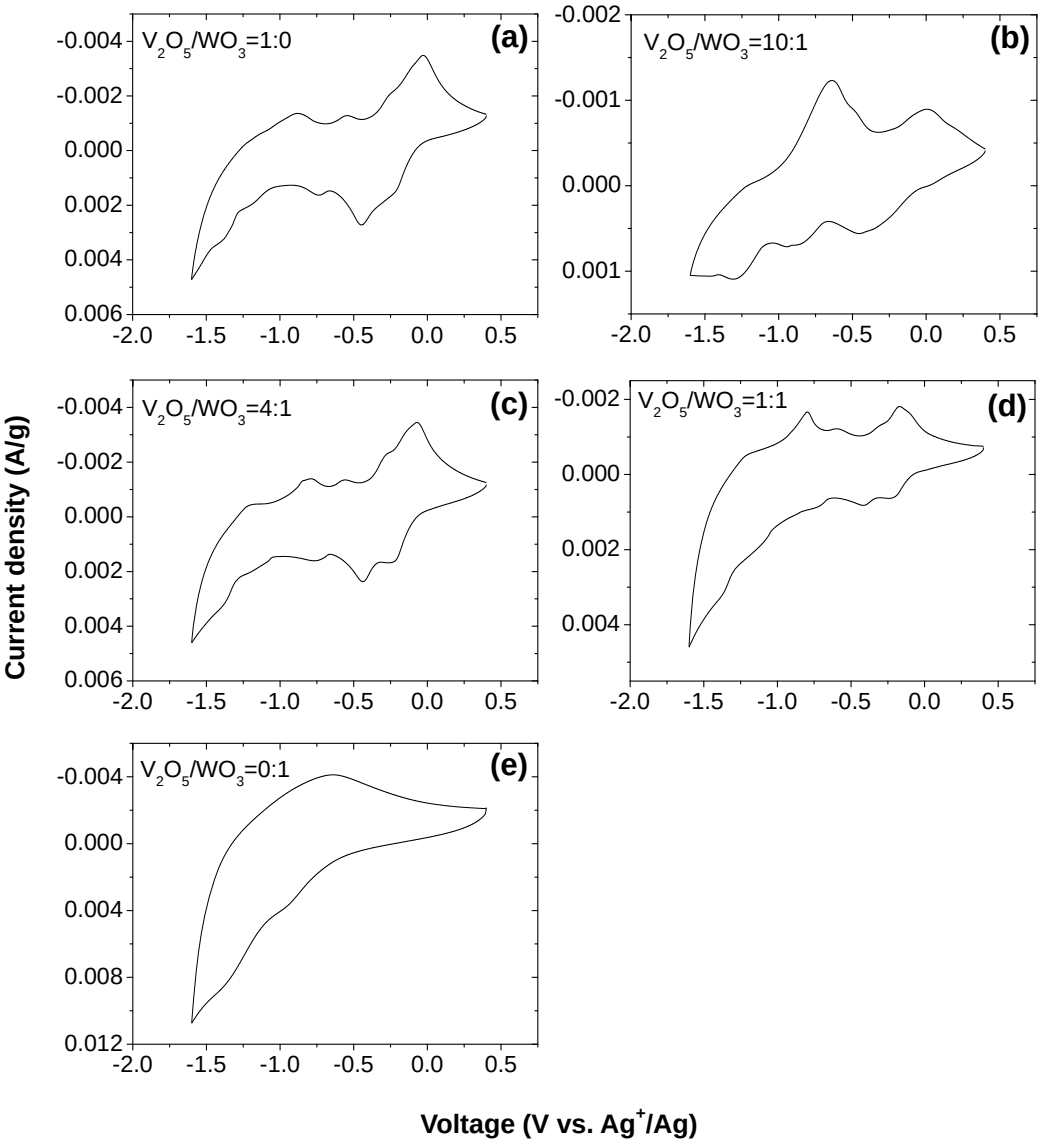

Figure 3.5 Cyclic voltammograms of V_2O_5 film, WO_3 film, and composite V_2O_5-WO_3 films with V_2O_5/WO_3= (a) 1:0, (b) 10:1, (c) 4:1, (d) 1:1 and (e) 0:1. The scan rate is 0.05 V/s.

However, the shoulder around -0.217 V becomes a more discernable peak in the curve of this composite film with a V_2O_5/WO_3 molar ratio of 4:1, indicating enhanced

kinetics for Li-ion intercalation in the composite film. For the film with a V_2O_5/WO_3 molar ratio of 1:1, two cathodic peaks are at -0.217 V, -0.421 V and three shoulders are around -0.706 V, -1.149 V and -1.370 V; three anodic peaks are at -0.170 V, -0.601 V, -0.794 V and two shoulders are around -0.304 V and -1.225 V. The positions of the cathodic peaks and shoulders are similar to those on the CV curve of pure V_2O_5, but the peaks are less discernable, indicating decreased kinetic property for Li-ion intercalation compared to the pure V_2O_5 film, which can be ascribed to the increase of the amount of WO_3. On the other hand, the anodic peak at -0.170 V shifts to a more negative position and the peak at -0.794 V shifts to a more positive position compared to the peaks in the curve of pure V_2O_5 film. The curve obtained by the composite film (V_2O_5:WO_3 = 10:1) exhibits a simpler and considerably different profile compared to the CV curve of pure V_2O_5 film: both anodic and cathodic peaks shift appreciably; the cathodic peaks shift to -0.463 V, -0.949 V and -1.307 V, and the anodic peaks and shoulders shift to -0.008 V, -0.482 V and -0.642 V. Not only the position of the peaks and shoulders shift obviously, but also the shape of them change appreciably, which indicates that phase transitions during electrochemical intercalation/deintercalation in this composite film are different from those occurring in the pure V_2O_5 film. Similar results have also been observed from chronopotentiometric measurements as discussed below.

Figure 3.6 illustrates the chronopotentiometric (CP) curves of the films heated at 470 ^oC with various V_2O_5/WO_3 molar ratios of 1:0, 10:1, 4:1, 1:1, 1:4 and 0:1 under a current density of 1.33 A/g. The CP curve of V_2O_5/WO_3=1:0 (pure V_2O_5) shows a

stepwise shape with two plateaus starting at -0.43 V and -1.22 V, which are ascribed to two phase changes of $Li_xV_2O_5$ during Li^+ intercalation [101, 124].

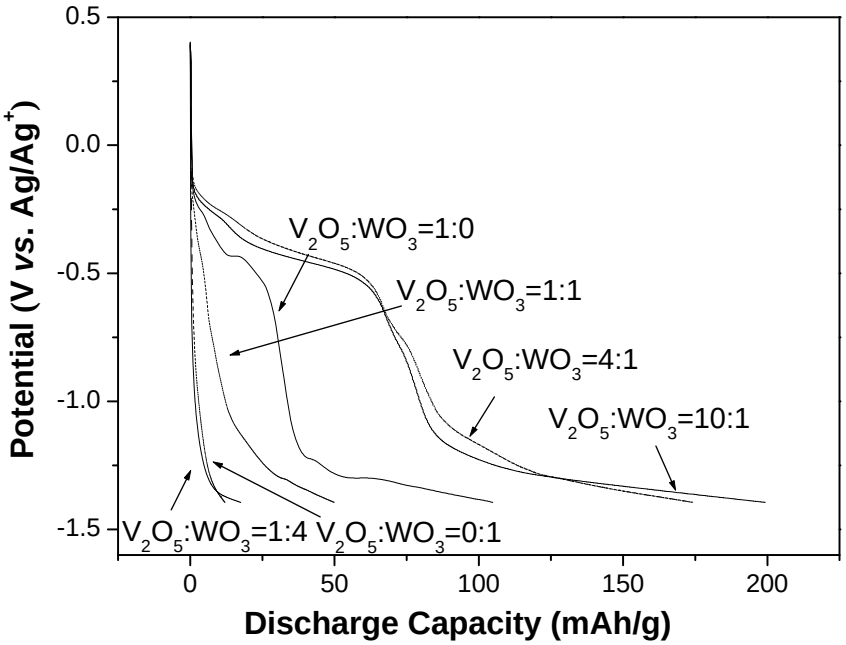

Figure 3.6 Chronopotentiometric curves of V_2O_5 film, WO_3 film, and composite V_2O_5-WO_3 films with various V_2O_5/WO_3 molar ratios, at a constant current density of 1.33 A/g.

On the other hand, the CP curve of WO_3 film shows a sloping shape without stages. The CP curves of composite films with V_2O_5/WO_3 molar ratios of 4:1 and 10:1 also show two plateaus, similar to those of pure V_2O_5, but the plateaus in the CP curve of the composite film are less distinct, suggesting the deterioration of crystallinity of V_2O_5 caused by WO_3. Both of these two composite films show enhancement of Li-ion intercalation in the first phase change process. However, the composite film with a molar ratio of V_2O_5/WO_3=10:1 delivers a higher capacity of 100 mA•h/g in the potential range of -1.22 V and -1.4 V, whereas the pure V_2O_5 film and the composite film with a molar ratio of V_2O_5/WO_3=4:1 deliver a similar capacity of 65 mA•h/g. The CP curves of composite films with V_2O_5/WO_3 molar ratios of

1:1 and 1:4 only have a gradual potential decrease without any distinct stepwise potential drop, similar to that of pure WO_3. Such disappearance of stepwise potential drop with increased WO_3 composition in the V_2O_5-WO_3 composite films further indicates the amorphization of V_2O_5 caused by addition of WO_3. As can be clearly seen from figure 3.6, the composite film with a V_2O_5/WO_3 molar ratio of 10:1 delivers the highest discharge capacity of 200 mA•h/g than all other films at the same current density of 1.33 A/g, for example, almost twice of that delivered by pure V_2O_5 film (108 mA•h/g). The coulombic efficiency of the composite film with a V_2O_5/WO_3 molar ratio of 10:1 is 70.5% which is slightly higher than that of the pure V_2O_5 film (67.5 %).

Figure 3.7 (a) summarizes the discharge capacity as a function of current density for pure V_2O_5 and WO_3 films, and various composite V_2O_5-WO_3 films. When a relatively small amount of WO_3 is added into V_2O_5 as in the case of composite films with V_2O_5/WO_3 molar ratios of 4:1 and 10:1, the discharge capacity can be enhanced compared to pure V_2O_5 film. However, the Li^+ intercalation capacity is reduced compared to that of pure V_2O_5 film, when too much WO_3 is added into V_2O_5 as in the case of composite film with a V_2O_5/WO_3 molar ratio of 1:1. The discharge capacity of the composite film is greatly reduced when WO_3 is the major composition and plays a dominant role. Figure 3.7 (b) shows the change of discharge capacity as a function of molar fraction of V_2O_5 (the moles of V_2O_5 divided by the total moles of V_2O_5 and WO_3) at different current densities. The discharge capacity first increases gradually with the increased amount of V_2O_5 in the composite films, but reaches the

highest value with the V_2O_5/WO_3 molar ratio of 10:1 showing 356 mA•h/g, 200 mA•h/g and 190 mA•h/g at current densities of 0.666 A/g, 1.333 A/g and 1.667 A/g, respectively. The trend of capacity *vs.* molar fraction is the same for all the three different current densities.

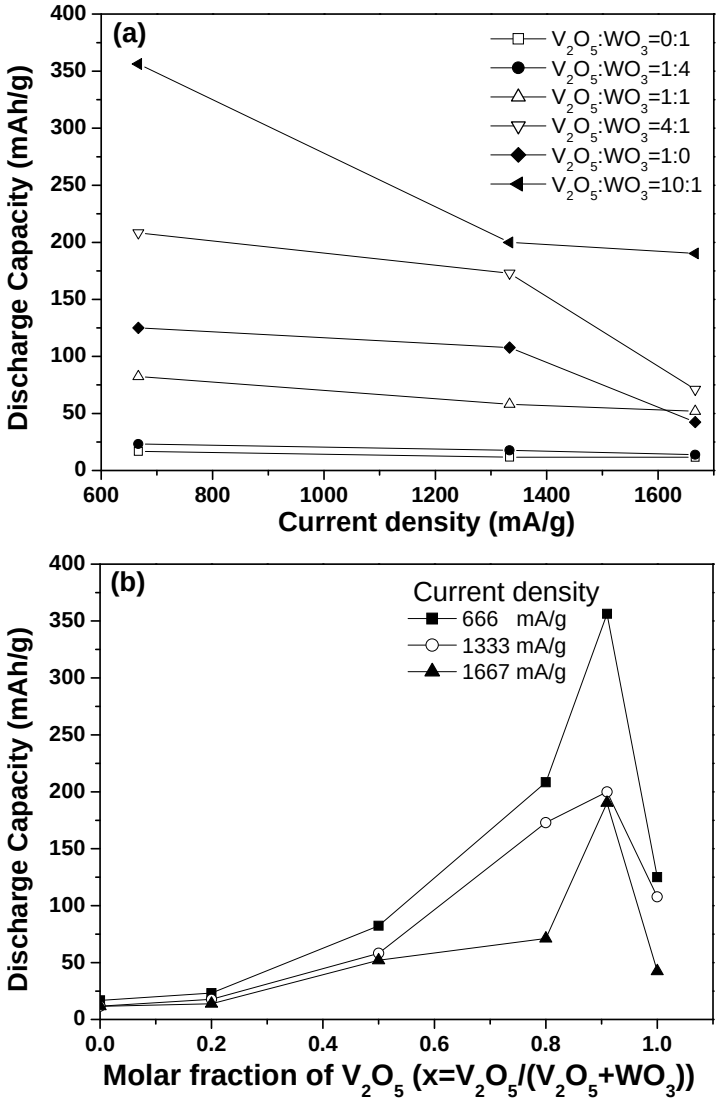

Figure 3.7 (a) Summary of the discharge capacities of various V_2O_5-WO_3 composite films (a) as a function of current density, and (b) as a function of molar fractions of V_2O_5 (the moles of V_2O_5 divided by the total moles of V_2O_5 and WO_3).

Figure 3.8 compares the cycling performances of pure V_2O_5, pure WO_3 and the composite films with different V_2O_5/WO_3 molar ratios at a current density of 1.33 A/g.

It can be seen that the composite film with a V_2O_5/WO_3 molar ratio of 10:1 delivers the highest capacity at every cycle compared to other samples. It shows the highest initial discharge capacity of 200 mA•h/g, and maintains a highest capacity of 132 mA•h/g after 50 cycles.

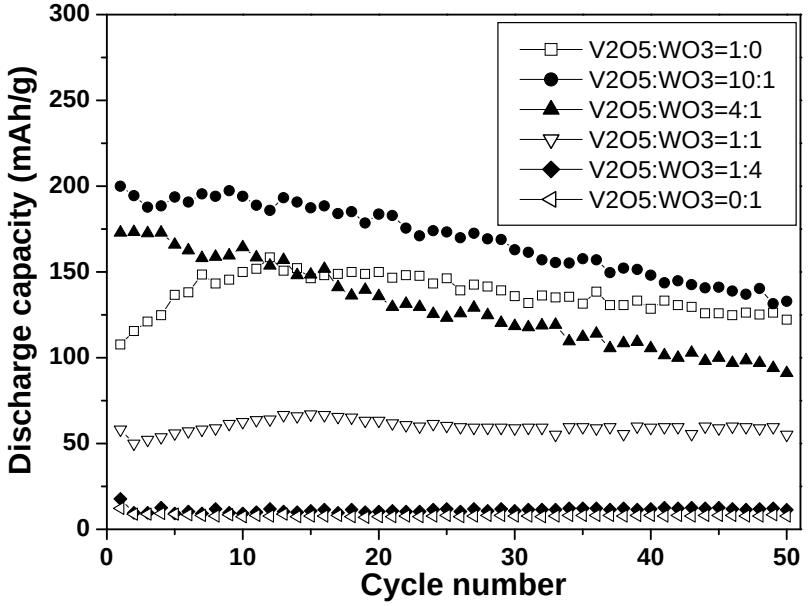

Figure 3.8 Cycling performances of V_2O_5 film, WO_3 film, and composite V_2O_5-WO_3 films with various V_2O_5/WO_3 molar ratios, at a current density of 1.33 A/g.

The cycling performance of pure V_2O_5 shows an increasing trend in initial cycles followed by degradation. The initial discharge capacity of pure V_2O_5 film is not high, but there is an increase of the discharge capacity between the 2nd cycle and the 13th cycle. Similar phenomena have been reported in literature [99]. The increase in initial capacities of V_2O_5 film can be attributed to the deterioration of crystallinity of V_2O_5 during initial cycling [99]. For the composite film with a V_2O_5/WO_3 molar ratio of 4:1, the initial capacity is higher than that of pure V_2O_5 film but lower than that of the composite film with a V_2O_5/WO_3 molar ratio of 10:1. However, this composite film with a molar ratio of 4:1 shows poor cycling performance. The

capacity decreases to 91 mA•h/g after 50 cycles, which is even lower than that of pure V_2O_5 film (122 mA•h/g). When the molar ratio of WO_3 increases gradually, the capacities delivered by the composite films (V_2O_5:WO_3 =1:1, 1:4, 0:1) decrease considerably, although the capacity retention is relatively stable. These results are due to the poor electrochemical activity of WO_3 in this potential range as discussed earlier.

The enhanced electrochemical properties of composite films can be attributed to the reduced grain size as shown in the XRD patterns (figure 3.1) and the increased porosity as shown in the SEM images (figure 3.3 and figure 3.4). Therefore, the composite film with smaller grain size provides larger electrochemical active surface area and shorter diffusion length for the Li-ion intercalation process. The composite films show an amorphous or partially amorphous phase from the XRD patterns in figure 3.1, which facilitates the intercalation of Li ions [125].

3.4 Summaries for V_2O_5-WO_3 Composite Films

V_2O_5-WO_3 composite films with enhanced intercalation properties have been prepared by a solution method without introducing any impurity elements. XRD, SEM and electrochemical measurements have been employed to reveal the structure and properties of these films. XRD analysis indicates that the addition of WO_3 greatly reduces the crystallinity of V_2O_5, which results in enhanced of Li-ion insertion capacities. SEM images show that fibers with different diameters are dispersed in porous films in the composite films, leading to higher surface area. Both the CV and CP curves of the V_2O_5-WO_3 film with the molar ratio of 10:1 are distinctively

different from those of V_2O_5 film, suggesting a different Li-ion intercalation process in the V_2O_5-WO_3 film with the molar ratio of 10:1. The V_2O_5-WO_3 film with the molar ratio of 10:1 delivers the highest discharge capacities of 200 mA•h/g at the first cycle and 132 mA•h/g after 50 cycles at a current density of 1.33 A/g, compared to pure oxide films and other composite films with different molar ratios; for example, the pure V_2O_5 film delivers only 108 mA•h/g at the first cycle at the same current density. The enhanced Li-ion intercalation properties of V_2O_5-WO_3 composite films are attributed to both morphological and structural changes in one oxide induced by the presence of other oxide.

Chapter 4 Surface Coating of $LiCoO_2$ by ALD for Li-Ion Batteries

4.1 Introduction to $LiCoO_2$

$LiCoO_2$ is the most popular among the possible cathode materials due to the ease of synthesis. $LiCoO_2$ can be prepared conveniently using solid state or wet chemical approaches [37-38]. It is found that mixing and heat-treated any precursors of lithium and cobalt can generate the oxide. For example, the oxide can be synthesized by heating a pelletized mixture of lithium carbonate and cobalt carbonate in air at 900°C for 20 h followed by two further heat treatments [126].

Extensive study has been conducted on Li_xCoO_2 system thus far and Li_xCoO_2 demonstrates excellent rechargeability at room temperature when $0.5 < x < 1$ [127-128]. At deep charge levels ($x < 0.5$), Li_xCoO_2 is chemically instable and the oxide begins to lose oxygen ions from its lattice due to a chemical reaction with the electrolyte [129-130], and thus the cycling performance is deteriorated significantly. Furthermore, there is an undesirable phase transformation to the monoclinic phase depending on the temperature in a small concentration interval of x= ~0.5. Specifically, the monoclinic phase exists approximately in the range $0.48 < x < 0.52$ at room temperature [127].

In order to improve the structural stability of $LiCoO_2$, coatings of carbon or various oxides have been studied and significant improvements in capacity retention have been demonstrated. Carbon-coating can enhance the structural stability and electrical conductivity of $LiCoO_2$ [131], but $LiCoO_2$ may be reduced to CoO or Co_3O_4 by carbon [132]. Apart from carbon coating, surface modification of $LiCoO_2$ by

coating various oxides such as ZrO_2 [77], Al_2O_3 [78], SnO_2 [79], MgO [80] and ZnO [43] has been widely investigated. The Al_2O_3-coated $LiCoO_2$ electrode exhibits excellent capacity retention among these oxide-coated electrodes. Two mechanisms have been proposed to explain the improved cycling performances of Al_2O_3-coated $LiCoO_2$ electrodes: (1) the Al_2O_3 serves as a separator to protect the direct contact between $LiCoO_2$ and the electrolyte, and thus suppresses the dissolution of the Co^{3+} into the electrolyte [133-134]; (2) The coating supplies a mechanical strength to endure the lattice variation of $LiCoO_2$ during the charge/discharge processes [135]. Different from Al_2O_3-coated $LiCoO_2$, ZnO-coated $LiCoO_2$ has received less attention. The ZnO coating can also improve the capacity retention of $LiCoO_2$ by reducing the cobalt dissolution and preventing the inorganic surface films such as LiF from covering the $LiCoO_2$ particles [43].

With the in-depth study of coated electrodes, it is feasible to optimize the properties of the coatings in order to improve the cycling performances further. Recently Yuhong Oh et al. reported that the cycling performance of $LiCoO_2$ is dependent on the coverage degree of Al_2O_3 coating, and a full coverage is optimal [47]. The thickness of the coating needs to be considered as well, since the coating reduces the fraction of electrochemical active material in the electrode and thick insulating coating such as Al_2O_3 coating significantly decreases the electronic conductivity of the electrode [136]. Al_2O_3 and ZnO coatings are usually synthesized by wet chemical methods following heat-treatment [40,134,137]. However, it is difficult to use these methods to coat a conformal layer of Al_2O_3 or ZnO on $LiCoO_2$

electrodes, and the thickness of the coatings is difficult to be controlled. In contrast, atomic layer deposition (ALD) is a gas-phase method. A conformal coating can be deposited on the electrodes by utilizing sequential self-limiting surface reactions [50]. The conformal coating using two ALD cycles has a thickness of only 3~4 Å, but the capacity retention increases from 45% for bare $LiCoO_2$ powders to 89% for Al_2O_3-coated $LiCoO_2$ powders after 120 electrochemical cycling measurements as reported by Yoon Seok Jung et al. [52]. The typical growth rate for Al_2O_3 and ZnO ALD is 1.1–1.2 Å [138] and 2.0 Å [139] per ALD cycle, respectively. Hence, the thickness of the coating can be conveniently controlled by adjusting the cycles of ALD.

In addition, coatings are more important for $LiCoO_2$ powders with small size such as nanosized and submicrosized powders. $LiCoO_2$ powders with smaller size can deliver larger capacity due to larger surface area. However, increased contact between $LiCoO_2$ and electrolyte aggravates the undesired reactions as well. In this work, ALD is utilized to deposit Al_2O_3 and ZnO coatings on $LiCoO_2$ electrodes comprised of submicrosized $LiCoO_2$ powders and the cycling performances of the coated $LiCoO_2$ electrodes are investigated in order to examine the effectiveness of the ultrathin conformal coatings.

4.2 Experimental Details

$LiCoO_2$ powders were prepared using a molten salt synthesis method reported by Juan Fu et al. [140]. A mixture of 10.000 g Co_3O_4 powder (99%, Alfa Aesar), 5.489 g $LiOH•H_2O$ powder (98%, Alfa Aesar) and 37.790 g KNO_3 powder (99.0%, Alfa Aesar)

were ground in a mortar until the color was uniform. Subsequently, the mixture was poured into an alumina crucible, moved into a muffle furnace and annealed at 600 ^{o}C in air for 8 h with heating and cooling rates of 10 ^{o}C/min. The resulting black powders were thoroughly washed with distilled water to remove residual $LiOH•H_2O$ and KNO_3. Finally, the precipitates obtained were dried at 100 ^{o}C in the furnace for 24 h. $LiCoO_2$ powder, carbon black and poly(vinylidene fluoride) (PVDF) were mixed in an agate mortar with a weight ratio of 83:7.5:9.5. 1-Methyl-2-pyrrolidinone as solvent was added to the mixture and black slurry was resulted. The composite electrode was made by spreading the slurry on a piece of Ti foil. Subsequently, the composite electrode was drying at 120 ^{o}C in vacuum for 9.5 h.

The Al_2O_3 layers were coated on the $LiCoO_2$ electrode by repeating two self-limiting surface reactions in which trimethylaluminum (TMA) and H_2O were used as precursors [138,141]:

$$AlOH^{*} + Al(CH_3)_3 \rightarrow AlO–Al(CH_3)_2^{*} + CH_4 \qquad (1)$$

$$AlO–Al(CH_3)_2^{*} + H_2O \rightarrow AlO–Al–OH^{*} + CH_4 \qquad (2)$$

In the case of ZnO ALD, diethylzinc (DEZ) and H_2O were used as the reactants. The two self-limiting surface reactions were [142-143]:

$$ZnOH^{*} + Zn(CH_2CH_3)_2 \rightarrow ZnO–Zn(CH_2CH_3)^{*} + CH_3CH_3 \qquad (3)$$

$$ZnO–Zn(CH_2CH_3)^{*} + H_2O \rightarrow ZnOH^{*} + CH_3CH_3 \qquad (4)$$

Figure 4.1 shows a schematic diagram of the ALD system (Savannah 100 & 200, Cambridge NanoTech Inc.). The electrodes were placed at the center of the reactor chamber (A). Precursors were stored in the cylinders (B) and (C), respectively. A

series of high-speed ALD pulse valves (D) and mass flow controller (E) respectively controlled the introduction of precursors and carrier gas (N_2) into the chamber.

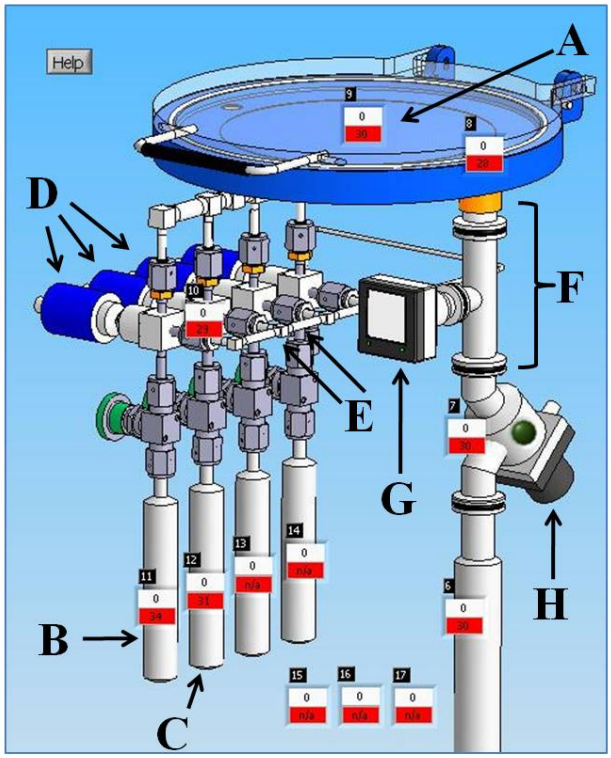

Figure 4.1 A schematic diagram of the ALD system.

The chamber was linked with a mechanical pump using a pumping line (F) in order to evacuate the chamber. There were a pressure gauge (G) used for measuring the pressure of the chamber and a stop valve (H) which controlled the connectivity between the chamber and the pumping line. The reactions occurred at a constant temperature by heating the reactor chamber at 140 ^{o}C. The cylinders containing precursors were not heated because the vapor pressures of TMA and DEZ were high enough for the ALD process. The ALD valves and the pumping line were heated to 100 ^{o}C in order to prevent the deposition of TMA or DEZ on them during the pulse and evacuation processes.

The Al_2O_3 or ZnO ALD reaction sequence was: (1) H_2O pulse (0.1 s); (2) H_2O reaction (30 s); (3) N_2 purge to evacuate excess H_2O (30 s); (4) TMA or DEZ pulse (0.01 s or 0.015 s); (5) TMA or DEZ reaction (5 s); (6) N_2 purge to evacuate by-products and excess TMA/DEZ (30 s).

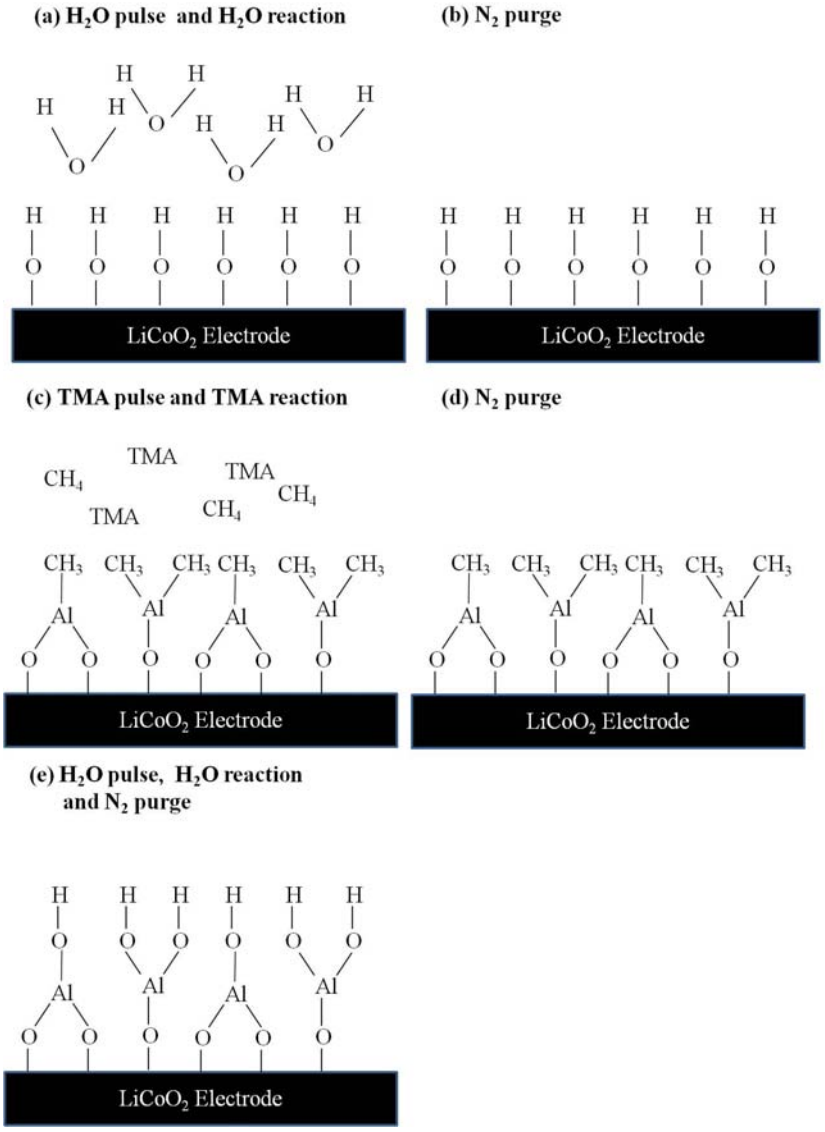

Figure 4.2 A schematic diagram of the growth of one Al_2O_3 layer by ALD.

Figure 4.2 shows the first layer of Al_2O_3 ALD. Figure 4.2 (a) shows a hydroxyl layer grow on the bare $LiCoO_2$ electrode after a H_2O pulse and the reaction between $LiCoO_2$ and H_2O. Figure 4.2 (b) shows the excess H_2O is purged by N_2. Figure 4.2

(c) and (d) show a layer of $AlO–Al(CH_3)_2^*$ grow on the $LiCoO_2$ electrode, and by-products (CH_4) and excess TMA are purged by N_2. Figure 4.2 (e) shows that a layer of $AlO–Al–OH^*$ is on the $LiCoO_2$ electrode after another H_2O pulse and N_2 purge. Four Al_2O_3 or ZnO layers were coated on bare $LiCoO_2$ electrode. After the ALD process, the coated electrode was gradually cooled to room temperature.

The crystalline phase of the bare $LiCoO_2$ electrode was analyzed by X-ray diffraction (XRD) using a Rigaku MiniFlex diffractometer with CuKα radiation operated at 30 kV and 15 mA. Scanning electron microscopy (SEM, Quantum 3D FEG) was used to examine the morphology of the bare $LiCoO_2$ powders. A three-electrode cell was used to investigate the electrochemical properties of the bare and coated $LiCoO_2$ electrodes on Ti foils. A platinum mesh was used as counter electrode and a silver wire in a 0.1 mol/L $AgNO_3$ ethanol solution served as the reference electrode. The electrolyte was a 1 mol/L solution of lithium perchlorate (99%, Alfa Aesar) in propylene carbonate (99%, Aldrich). The galvanostatic charge–discharge cycling measurements were carried out at a potential limit of -0.3 and 0.9 V versus Ag/Ag^+ under a current density of 140 mA/g using a potentiostat/galvanostat (Model 605C, CH Instrument).

4.3 Results and Discussion

Figure 4.3 shows the XRD pattern of the $LiCoO_2$ powders produced by solid-state reaction of Co_3O_4, $LiOH·H_2O$ and KNO_3. It can be clearly seen that there are several diffraction peaks in the pattern, such as (003) peak at $2\theta=18.7^o$ and (104) peak at $2\theta=45.1^o$. All the peaks are indexed to $LiCoO_2$ (JCPDS card No. 16-0427). $LiCoO_2$ has

a layered structure described by the space group R-3m(166). In this structure, a trigonal unit cell consisting of a cubic close packed oxygen lattice with Li^+ ions and Co^{3+} ions occupying two sets of octahedral interstitial sites respectively (O 6c sites, Li 3a sites, Co 3b sites) [37]. Due to the strong ionicity of the Co-O bond, the lattice can be regarded as slabs of edge sharing CoO_6 octahedra that are separated by layers of Li^+ ions [144].

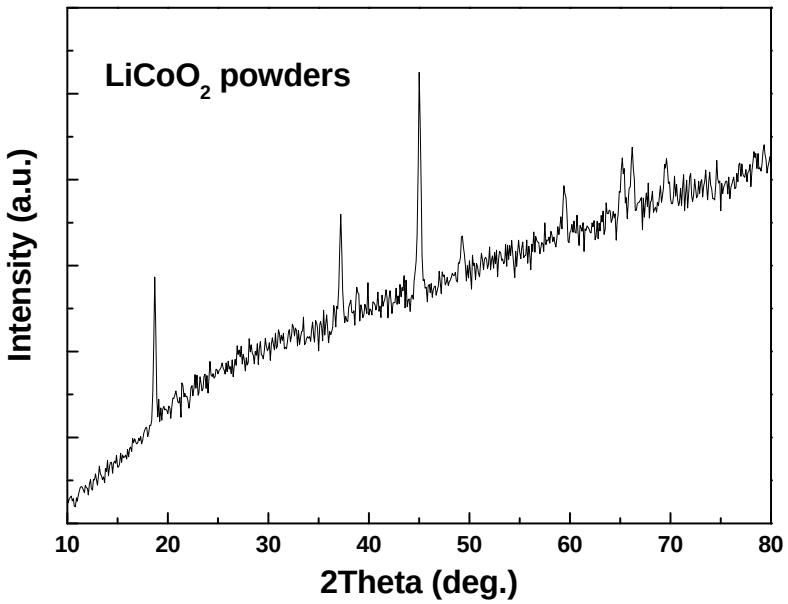

Figure 4.3 X-ray diffraction pattern of the $LiCoO_2$ powders prepared by solid-state reaction.

Figure 4.4 shows top-view SEM images of Co_3O_4 powders and the as-synthesized $LiCoO_2$ powders. A lithiation process occurred in this molten salt synthesis method and thus the $LiCoO_2$ crystal grew up with Co_3O_4 as core [140]. Therefore, the $LiCoO_2$ powders show similar particle sizes to the Co_3O_4 powders and most of the powders agglomerate together. These $LiCoO_2$ powders are polygonal particles with broad particle size distribution. The diameters of the particles range from ~300 nm to ~750 nm. Particles with smaller diameters have larger surface area and resulting enhanced

electrochemical activity. However, the contact area between $LiCoO_2$ and the electrolyte is enlarged as well, and thus the dissolution of Co^{3+} and the side reaction between $LiCoO_2$ and the electrolyte are facilitated, which will deteriorate the cycling performance.

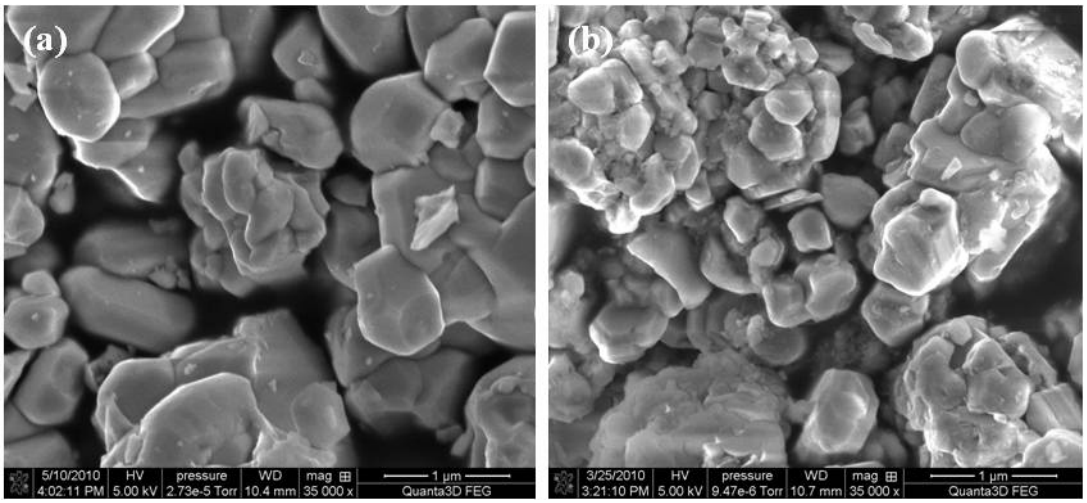

Figure 4.4 SEM micrographs showing surface morphologies of (a) Co_3O_4 powders and (b) as-synthesized $LiCoO_2$ powders.

Figure 4.5 compares the cycling performances of bare, Al_2O_3-coated and ZnO-coated $LiCoO_2$ electrodes in the range of -0.3–0.9 V (vs. Ag/Ag^+) with a current density of 140 mA/g in first 20 cycles. The bare $LiCoO_2$ electrode delivers the highest initial discharge capacity of 93.0 mA•h/g compared to those delivered by the Al_2O_3-coated $LiCoO_2$ electrode (81.4 mA•h/g) and ZnO-coated $LiCoO_2$ electrode (78.9 mA•h/g). The lower initial capacities of the coated electrodes are ascribed to the poor electronic conductivity of Al_2O_3 and ZnO coatings. However, the capacity retention of the bare $LiCoO_2$ electrode fades rapidly: it delivers discharge capacities of 21.3 mA•h/g after 10 cycles and 9.1 mA•h/g after 20 cycles. Although the capacity delivered by Al_2O_3-coated $LiCoO_2$ electrode is lower than bare $LiCoO_2$ electrode in

the initial four cycles, the Al_2O_3-coated $LiCoO_2$ electrode shows improved cycling performance compared to the bare $LiCoO_2$ electrode.

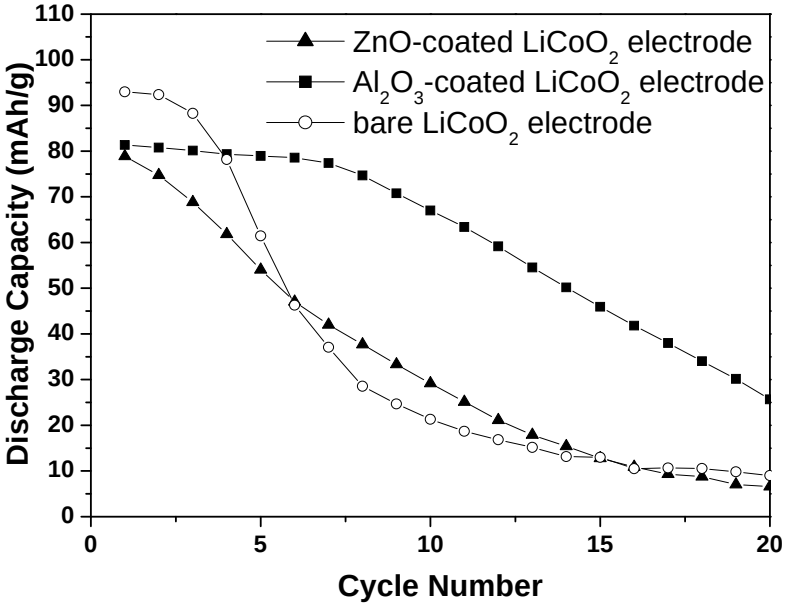

Figure 4.5 Cycle performances of bare, Al2O3-coated, and ZnO-coated $LiCoO_2$ electrodes at a current density of 140 mA/g.

For example, the Al_2O_3-coated $LiCoO_2$ electrode can deliver discharge capacities of 67.0 mA•h/g after 10 cycles and 25.9 mA•h/g after 20 cycles. In contrast, the ZnO-coated $LiCoO_2$ electrode does not exhibit enhanced capacity retention compared to the bare $LiCoO_2$ electrode. The ZnO-coated $LiCoO_2$ electrode delivers a slightly higher capacity of 29.2 mA•h/g at the 10th cycle, but it delivers 6.6 mA•h/g at the 20th cycle which is even lower than that delivered by the bare $LiCoO_2$ electrode at the same cycle.

Figure 4.6 compares the chronopotentiometric (CP) curves of the Al_2O_3-coated, ZnO-coated and bare $LiCoO_2$ electrodes at 1st, 5th and 10th discharge processes. The curves of the bare $LiCoO_2$ electrodes show a stage starting at ~0.24 V in the 1st discharge process as shown in figure 4.6 (a), indicating a phase transition occurs

during the Li-ion intercalation process. However, the stage disappears in the curves at the 5th and 10th cycle, indicating the deterioration of crystallinity of the bare $LiCoO_2$.

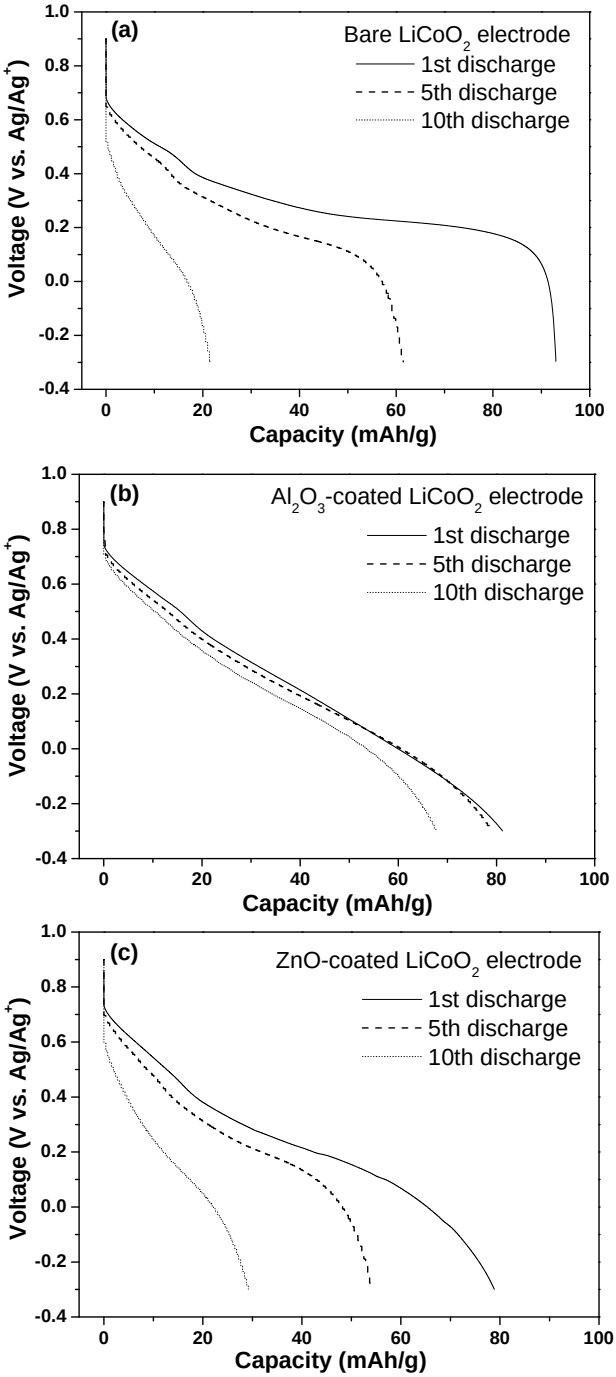

Figure 4.6 The 1st, 5th and 10th discharge voltage profiles of bare, Al_2O_3-coated and ZnO-coated $LiCoO_2$ electrodes at a current density of 140 mA/g.

In addition, the curves of the bare $LiCoO_2$ electrode exhibit large overpotential with the increase of the cycle number, which is ascribed to large polarization of the bare $LiCoO_2$ electrode. On the other hand, the curves of the Al_2O_3-coated $LiCoO_2$ electrode show a sloping shape without stages, and the polarization of the Al_2O_3-coated $LiCoO_2$ electrode is inhibited as shown in figure 4.6 (b). Figure 4.6 (c) shows that the ZnO-coated $LiCoO_2$ electrode shows similar CP curves with the bare $LiCoO_2$ electrode: large overpotentials are observed in the CP curves and the capacity retention fades rapidly.

As mentioned in the introduction section, there are two possible mechanisms for the enhanced capacity retention of the $LiCoO_2$ electrodes coated by Al_2O_3. In this work, the Al_2O_3 coating is ultrathin, so it cannot offer enough mechanical strength to suppress the lattice change caused by the phase transition during the electrochemical measurements. However, this conformal coating can indeed prevent the direct contact between $LiCoO_2$ and the electrolyte, and thus suppress the dissolution of Co^{3+} and the side reaction with electrolyte. In contrast, the ZnO coating does not improve the cycling performance of the $LiCoO_2$ electrode, because it is not electrochemical stable [48].

4.4 Summaries for Surface Coating of $LiCoO_2$ Electrodes

Ultrathin conformal Al_2O_3 and ZnO films are coated on $LiCoO_2$ electrodes by ALD. The Al_2O_3-coated $LiCoO_2$ electrode exhibits improve cycling stability during the electrochemical measurements, while the ZnO-coated $LiCoO_2$ electrode does not show an improved cycling performance. For example, the Al_2O_3-coated $LiCoO_2$

electrode can deliver discharge capacities of 67.0 mA•h/g after 10 cycles and 25.9 mA•h/g after 20 cycles, while the bare $LiCoO_2$ electrode delivers discharge capacities of 21.3 mA•h/g after 10 cycles and 9.1 mA•h/g after 20 cycles, and the ZnO-coated $LiCoO_2$ electrode delivers capacities of 29.2 mA•h/g at the 10th cycle and 6.6 mA•h/g at the 20th cycle.

Chapter 5 Concluding Remarks

This thesis reports enhanced Li-ion intercalation properties of V_2O_5-WO_3 composite films and $LiCoO_2$ electrode with nanosized thin coating.

A solution method has been applied to prepared V_2O_5-WO_3 composite films without introducing any impurity elements. The V_2O_5-WO_3 composite film with a V_2O_5/WO_3 molar ratio of 10:1 exhibits enhanced discharge capacities due to the amorphous structure and larger surface area as indicated by XRD analysis and SEM images, respectively. A different Li-ion intercalation process in the V_2O_5-WO_3 film is observed as shown in the CV and CP curves. The V_2O_5-WO_3 film with the molar ratio of 10:1 delivers the highest discharge capacities of 200 mA•h/g at the first cycle and 132 mA•h/g after 50 cycles at a current density of 1.33 A/g, compared to pure oxide films and other composite films with different molar ratios; for example, the pure V_2O_5 film delivers a capacity of only 108 mA•h/g at the first cycle at the same current density. The enhanced Li-ion intercalation properties of V_2O_5-WO_3 composite films are attributed to both morphological and structural changes in one oxide induced by the presence of other oxide.

The conformal ultrathin surface coating on $LiCoO_2$ are achieved by atomic layer deposition. The Al_2O_3-coated $LiCoO_2$ electrode exhibits enhanced capacity retention during the electrochemical cycling measurements due to the inhibition of cobalt dissolution and side reaction. In contrast, the ZnO-coated $LiCoO_2$ electrode does not show an improved cycling performance due to the electrochemical instability of the ZnO coating. For example, the Al_2O_3-coated $LiCoO_2$ electrode delivers a discharge

capacity of 67.0 mA•h/g after 10 cycles, while the bare and ZnO-coated $LiCoO_2$ electrodes deliver discharge capacities of 21.3 mA•h/g and 29.2 mA•h/g after 10 cycles, respectively.

References

[1] G. Li, V. Shrotriya, J.S. Huang, Y. Yao, T. Moriarty, K. Emery, Y. Yang, Nat. Mater. 4 (2005) 864.

[2] Advances in Lithium-Ion Batteries; eds. W. van Schalkwijk, B. Scrosati, Springer, 2002.

[3] J. M. Tarascon, M. Armand, Nature 414 (2001) 359.

[4] M. Winter, R.J. Brodd, Chem. Rev. 104 (2004) 4245.

[5] D. O'Hare, Inorganic Materials, eds. D. W. Bruce, D. O'Hare, John Wiley & Sons: New York, p. 165, 1991.

[6] R. Schöllhorn, Angew Chem. Int. Ed. Engl. 19 (1980) 983.

[7] R. Schöllhorn, Chemical Physics of Intercalation, A. P. Legrand, S. Flandrois, Plenum, New York, NATO Ser. B 172 (1987) 149.

[8] D. W. Murphy, S. A. Sunshine, S. M. Zahurak, in Chemical Physics of Intercalation, eds. A. P. Legrand, S. Flandrois, Plenum: New York, NATO Ser. B 172 (1987) 173.

[9] D. W. Murphy, P. A. Christian, F. J. Disalvo, J. V. Waszczak, Inorg. Chem. 24 (1985) 1782.

[10] R. Clement, J. Am. Chem. Soc. 103 (1981) 6998.

[11] L. F. Nazar, A. J. Jacobson. J. Chem. Soc. Chem. Commun. (1986) 570.

[12] R. Schöllhorn, Physics of Intercalation Compounds; Springer-Verlag: Berlin, 1981.

[13] A. S. Aricò, P. Bruce, B. Scrosati, J-M. Tarascon, W. V. Schalkwijk, Nat. Mater. 4 (2005) 366.

[14] D. W. Murphy, P. A. Christian, F. J. DiSalvo, J. V. Waszczak, Inorg. Chem. 18 (1979) 2800.

[15] L. Abello, E. Husson, Y. R. Repelin, G. Lucazeau, Spectrochim. Acta, 39A (1983) 641.

[16] M. S.Whittingham, J. Electrochem. Soc. 123 (1976) 315.

[17] J. M. Cocciantelli, J. P. Doumerc, M. Pouchard, M. Broussely, J. Labat, J. Power Sources, 34 (1991) 103.

[18] J. J. Galy, Solid State Chem. 100 (1992) 229.

[19] R. J. Cava, A. Santoro, D. W. Murphy, S. M. Zahurak, R. M. Fleming, P. Marsch, R. S. J. Roth, Solid State Chem. 65 (1986) 63.

[20] M. Broussely, J. Labat, J. M. Bodet, J. M. Cocciantelli, J. Power Sources 13 (1991) 429.

[21] J. Labat, J. M. Cocciantelli, French Patent 8916337, 1989.

[22] C. Delmas, H. Cognac-Auradou, J. M. Cocciantelli, M. Ménétrier, J. P. Doumerc, Solid State Ionics 69 (1994) 257.

[23] C. Delmas, S. Br.thes, M. Ménétrier, J. Power Sources 34 (1991) 113.

[24] C. Delmas, in "Lithium Batteries: New Materials, Developments and Perspectives" (Ed: G. Pistoia), Elsevier, Amsterdam 1994, p. 457.

[25] K. West, B. Zachau-Christiansen, M. J. L. Ostergard, T. Jacobsen, J. Power Sources 20(1-2) (1987) 165.

[26] K. West, B. Zachau-Christiansen, T. Jacobsen, S. Skaarup, Electrochim. Acta 38 (1993) 1215.

[27] K. Salloux, F. Chaput, H. P. Wong, B. Dunn, M. W. Breiter, J. Electrochem. Soc. 142(10) (1995) L191.

[28] T. Watanabe, Y. Ikeda, T. Ono, M. Hibino, M. Hosoda, K. Sakai, T Kudo, Solid State Ionics 151 (2002) 313.

[29] F. Coustier, J. Hill, B. B. Owens, S. Passerini, W. H. Smyrl, J. Electrochem. Soc. 146 (1999) 1355.

[30] Livage, J. Chem. Mater. 3 (1991) 578.

[31] Y. Dimitriev, V. Dimitrov, M. Arnaudov, D. J. Topalov, Non-Cryst. Solids 57 (1983) 147.

[32] N. Machida, R. Fuchida, T. Minami, J. Electrochem. Soc. 136 (1989) 2133.

[33] S. Y. Zhan, C. Z. Wang, K. Nikolowski, H. Ehrenberg, G. Chen, Y.J. Wei, Solid State Ionics 180 (2009) 1198.

[34] M. J. Parent, S. Passerini, B. B. Owens, W. H. Smyrl, J. Electrochem. Soc. 146 (1999) 1346.

[35] T. Kudo, Y. Ikeda, T. Watanabe, M. Hibino, M. Miyayama, H. Abe, K. Kajita, Solid State Ionics 152-153 (2002) 833.

[36] D. Zhu, H. Liu, L. Lv, Y. D. Yao, W. Z. Yang, Scripta Mater. 59 (2008) 642.

[37] J. N. Reimers, J. R. Dahn, J. Electrochem. Soc. 139 (1992) 2091.

[38] P. N. Kumta, D. Gallet, A. Waghray, G. E. Blomgren, M. P. Setter, J. Power Sources 72 (1998) 91.

[39] J. Y. Liu, N. Liu, D. T. Liu, Y. B., L. H. Shi, Z. X. Wang, L. Q. Chen, V. Hennige, A. Schuch, J. Electrochem. Soc. 154 (1) (2007) A55.

[40] L. J. Liu, Z. X. Wang, H. Li, L. Q. Chen, X. J. Huang, Solid State Ionics 152–153 (2002) 341.

[41] H. Li, Z. X Wang, L. Q. Chen, and X. J. Huang, Adv. Mater. 21 (2009) 4593.

[42] G. G. Amatucci, J. M. Tarascon, L. C. Klein, Solid State Ionics 83 (1996) 167.

[43] T. Fang, J. Duh, S. J. Sheen, Electrochem. Soc. 152 (2005) A1701.

[44] J. Tu, X.B. Zhao, G.S. Cao, D.G. Zhuang, T.J. Zhu, J.P. Tu, Electrochim. Acta 51 (2006) 6456.

[45] S.-W. Lee, K.-S. Kim, H.-S. Moon, H.-J. Kim, B.-W. Cho, W.-Il Cho, J.-B. Ju, J.-W. Park, J. Power Sources 126 (2004) 150.

[46] T. Okumuraa, T. Fukutsukaa, Y. Uchimotoa, K. Amezawab, S. Kobayashic, J. Power Sources 189 (2009) 471.

[47] Y. Oh, D. Ahn, S. Nam and B. Park, J Solid State Electrochem. 14 (2010) 1235.

[48] Y. S. Jung, A. S. Cavanagh, A. C. Dillon, M. D. Groner, S. M. George, and S.-H. Lee, J. Electrochem. Soc. 157 (1) (2010) A75.

[49] T. Suntola, Thin Solid Films 216 (1992) 84.

[50] S. M. George, A. W. Ott, J. W. Klaus, J. Phys. Chem. 100 (1996) 13121.

[51] R. Beetstra, U. Lafont, J. Nijenhuis, E. M. Kelder, and J. Ruud van Ommen, Chem. Vap. Deposition 15 (2009) 227.

[52] Y. S. Jung, A. S. Cavanagh, L. A. Riley, S.-H. Kang, A. C. Dillon, M. D. Groner, S. M. George, and S.-H. Lee, Adv. Mater. 22 (2010) 1.

[53] O. Sneh, R. B. Clark-Phelps, A. R. Londergan, J. Winkler, and T. E. Seidel, Thin Solid Films 402(1-2) (2002) 248.

[54] J. W. Elam, D. Routkevitch, P. P. Mardilovich, and S. M. George, Chem. Mater. 15(18) (2003**)** 3507.

[55] M. Scharrer, Ph. D. Dissertation, Northwestern University, Evanston, IL, 2007.

[56] M. Koltypin, V. Pol, A. Gedanken, D. Aurbach, J. Electrochem. Soc. 154 (2007) A605.

[57] J. S. Sakamoto, B. Dunn, J. Electrochem. Soc. 149 (2002) A26.

[58] A. Kuwahara, S. Suzuki, M. Miyayama, Solid State Ionics 179 (2008) 1890.

[59] I. Stojkovic, N. Cvjeticanin, S. Markovic, M. Mitric and S. Mentus, Acta Phys. Pol. A 117 (2010) 837.

[60] I. Boyano, M. Bengoechea, I. de Meatza, O. Miguel, I. Cantero, E. Ochoteco, J. Rodr´ıguez, M. Lira-Cant´u, P. G´omez-Romero, J. Power Sources 166 (2007) 471.

[61] M. Ferreira, V. Zucolotto, F. Huguenin, R M. Torresi, Jr. O. N. Oliveira, J. Nanosci. Nanotechnol. 2 (2002) 29.

[62] F. Huguenin, Jr. D. S. dos Santos, A. Bassi, F. C. Nart, Jr. O. N. Oliveira, Adv. Funct. Mater. 14 (2004) 985.

[63] E. A. Ponzio, T. M. Benedetti, R. M. Torresi, Electrochim. Acta, 52 (2007) 4419.

[64] C. V. S. Reddy, W. Jin, Q-Y. Zhu, W. Chen, R. R. Kalluru, Eur. Phys. J. Appl. Phys. 38 (2007) 31.

[65] K.Takahashi, Y. Wang, G. Z. Cao, J. Phys. Chem. B 109（2005）48.

[66] Y. Wang, K. Lee, H. Shang, B. Wiley, Y. Xia, G. Cao, A Phys. Stat. Sol. (a) 202 (2005) R79.

[67] M. G. Minett, J. R. Owen, J. Power Sources 32 (1990) 81.

[68] A. Davies, R. J. Hobson, M. J. Hudson, W. J. Macklin, R. J. Neat, J. Mater. Chem. 6 (1996) 49.

[69] N. Ozer, S. Sabuncu, J. Cronin, Thin Solid Films 338 (1999) 201.

[70] M.B. Sahan, C. Sudakar, C. Thapa, V.M. Naik, G.W. Auner, R. Naik, K.R. Padmanabhan, Thin Solid Films 517 (2009) 6642.

[71] K. Lee, G.Z. Cao, J. Phys. Chem. B 109 (2005) 11880.

[72] K. Takahashi, Y. Wang, K. Lee, G. Cao, Appl. Phys. A 82 (2006) 27.

[73] G. Li, Z. Yang, W. Yang, J. Power Sources 183 (2008) 741.

[74] J. Kim, M. Noh, J. Cho, H. Kim, K. Kim, J. Electrochem. Soc. 1526 (2005) A1142.
[75] J. Cho, B. Kim, J. Lee, Y. Kim, B. Park, J. Electrochem. Soc. 152 (2005) A32.

[76] B. Kim, C. Kim, T. Kim, D. Ahn, B. Park, J. Electrochem. Soc. 1539 (2006) A1773.

[77] Y. J. Kim, J. Cho, T. J. Kim, B. Park, J. Electrochem. Soc. 150 (2003) A1723.

[78] L. Lui, Z. Wang, H. Li, L. Chen, X. Huang, Solid State Ionics 152-153 (2002) 341.

[79] J. Cho, C.S. Kim, S. I. Yoo, Electrochem. Solid-State Lett. 3 (2000) 362.

[80] Z. X. Wang, X. J. Huang, L.Q. Chen, J. Electrochem. Soc. 150(2) (2003) A199.

[81] K. Y. Chung, W. Yoon, J. McBreen, X. Yang, S. H. Oh, H. C. Shin, W. I. Cho, B. W. Cho, J. Electrochem. Soc. 153 (2006) A2152.

[82] H. Miyashiro, A. Yamanaka, M. Tabuchi, S. Seki, M. Nakayama, Y. Ohno, Y. Kobayashi, Y. Mita, A. Usami, M.Wakihara, J. Electrochem. Soc. 153 (2006) A348.

[83] C.-Z. Lu, J.-M. Chen, Y.-D. Cho, W.-H. Hsu, P. Muralidharan, T.-K. Fey, J. Power Sources 184 (2008) 392.

[84] B. Kang, G. Ceder, Nature 458 (2009) 190.

[85] W. Wu, Y. Wang, X. Y. Wang, Q. Q. Chen, X. Wang, S. Y. Yang, X. M. Liu, J. Guo, Z. H. Yang, J. Alloys Compd. 486 (2009) 93.

[86] Y.-C. Si, L.-F. Jiao, H.-T. Yuan, H.-X. Li, Y.-M. Wang, J. Alloys Compd. 486 (2009) 400.

[87] A. Y. Shenouda, H. K. Liu, J. Alloys Compd. 477 (2009) 498.

[88] S. B. Tang, M. O. Lai, L. Lu, J. Alloys Compd. 449 (2008) 300.

[89] F. Teng, S. Santhanagopalan, Y. Wang, D. D. Meng, J. Alloys Compd. 499 (2010) 259.

[90] W. Huang, S. K. Gao, X. K. Ding, L. L. Jiang, M. D. Wei, J. Alloys Compd. 495 (2010) 185.

[91] Q. T. Qu, Y. Shi, L. L. Li, W. L. Guo, Y. P. Wu, H. P. Zhang, S.Y. Guan, R. Holze, Electrochem. Commun. 11 (2009) 1325.

[92] W.-C. Fang, J. Phys. Chem. C 112 (2008) 11552.

[93] C. G. Granqvist, Handbook of Inorganic Electrochromic Materials, Elsevier, Amsterdam, 1995.
[94] N. A. Galiote, F. Huguenin, J. Phys. Chem. C 111 (2007) 14911.

[95] A.Wolcott, T. R. Kuykendall, W. Chen, S. Chen, J. Z. Zhang, Phys. Chem. B 110 (2006) 25288.

[96] M. S. Whittingham, Chem. Rev. 104 (2004) 4271.

[97] C. Navone, J. P. Pereira-Ramos, R. Baddour-Hadjean, R. Salot, J. Power Sources 146 (2005) 327.

[98] Y. Wang, G. Z. Cao, Adv. Mater. 20 (2008) 2251.

[99] D. Liu, Y. Y. Liu, B. B. Garcia, Q. F. Zhang, A. Q. Pan, Y.-H. Jeong, G. Z. Cao, J. Mater. Chem. 19 (2009) 8789.

[100] A. Q. Pan, D.W. Liu, X. Y. Zhou, B. B. Garcia, S. Q. Liang, J. Liu, G. Z. Cao, J. Power Sources 195 (2010) 3893.

[101] F. Lantelme, A. Mantoux, H. Groult, D. J. Lincot, J. Electrochem. Soc. 150 (2003) A1202.

[102] K. E. Swider-Lyons, C. T. Love, D. R. Rolison, Solid State Ionics 152-153 (2002) 99.

[103] V. M. Mohan, B. Hu, W. L. Qiu, W. Chen, J. Appl. Electrochem. 39 (2009) 2001.

[104] C. R. Xiong, A. E. Aliev, B. Gnade, K. J. Balkus, Jr., ACS Nano 2 (2008) 293.

[105] A. P. Jin, W. Chen, Q. Y. Zhu, Y. Yang, V. L. Volkov, G. S. Zakharova, Thin Solid Films 517 (2009) 2023.

[106] M. Deepa, D. P. Singh, S. M. Shivaprasad, S. A. Agnihotry, Curr. Appl. Phys. 7 (2007) 220.

[107] C. G. Granqvist, Sol. Energy Mater. Sol. Cells 60 (2000) 201.

[108] J. M. Wang, E. Khoo, P. S. Lee, J. Ma, J. Phys. Chem. C 112 (2008) 14306.

[109] S. K. Deb, Sol. Energy Mater. Sol. Cells 92 (2008) 245.

[110] N. Ozer, C. M. Lampert, Thin Solid Films 349 (1999) 205.

[111] D.-W. Kim, H. Kim, Y.-S. Jung, I. K. Song, S.-H. Baeck, J. Phys. Chem. Solids 69 (2008) 1513.

[112] M. Najbar, F. Mizukami, P. Kornelak, A. Wesełucha-Birczy´nska, B. Borz¸ecka-Prokop, E. Biela´nska, A. Białas, J. Bana´s, D. Su, Catal. Today 90 (2004) 93.

[113] M. Ranjbar, S. M. Mahdavi, A. Iraji zad, Sol. Energy Mater. Sol. Cells 92 (2008) 878.

[114] G. J. Fang, K.-L. Yao, Z.-L. Liu, Thin Solid Films 394 (2001) 64.

[115] G. N. Barbosa, A. T. Bolsoni, H. P. Oliveira, J. Non-Cryst. Solids 354 (2008) 3548.

[116] C. J. Fontenot, J. W. Wiench, M. Pruski, G. L. J. Schrader, Phys. Chem. B 104 (2000) 11622.

[117] B. Yebka, B. Pecquenard, C. Julien, J. Livage, Solid State Ionics 104 (1997) 169.

[118] E. I. Rogers, D. S. Silvester, S. E. W. Jones, L. Aldous, C. Hardacre, A. J. Russell, S. G. Davies, R. G. Compton, J. Phys. Chem. C 111 (2007) 13957.

[119] E. Abitelli, S. Ferrari, E. Quartarone, P. Mustarelli, A. Magistris, M. Fagnoni, A. Albini, C. Gerbaldi, Electrochim. Acta 55 (2010) 5478.

[120] G. J. Fang, Z. L. Liu, Y. Q. Wang, H. H. Liu, K. L. J. Yao, Phys. D: Appl. Phys. 33 (2000) 3018.

[121] M. Yagia, S. Maruyamaa, K. Sonea, K. Nagaib, T. Norimatsu, J. Solid State Chem. 181 (2008) 175.

[122] X. L. Sun, H. T. Cao, Z. M. Liu, J. Z. Li, Appl. Surf. Sci. 255 (2009) 8629.

[123] W.-J. Li, Z.-W. Fu, Appl. Surf. Sci. 256 (2010) 2447.

[124] C. J. Patrissi, C. R. J. Martin, Electrochem. Soc. 146 (1999) 3176.

[125] F. Coustier, S. Passerini, W. H. Smyrl, Solid State Ionics 100 (1997) 247.

[126] K. Mizushima, P.C. Jones, P.J. Wiseman, J.B. Goodenough, Mater. Res. Bull. 15 (1980) 783.

[127] T. Ohzuku, A. Ueda, N. Nagayama, Y. Iwakoshi, H. Komori, Electrochim. Acta, 38 (1993) 1159.

[128] G.G. Amatucci, J.M. Tarascon, L.C. Klein, J. Electrochem. Soc. 143 (1996) 1114.

[129] R.V. Chebiam, F. Prado, A. Manthiram, Chem. Mater. 13 (2001) 2951.

[130] R.V. Chebiam, A. M. Kannan, F. Prado, A. Manthiram Electrochem. Commun. 3 (2001) 624.

[131] H. Liu, C. Li, H.P. Zhang, L.J. Fu, Y.P. Wu, H.Q. Wu, J. Power Sources 159 (2006) 717.

[132] H. Takahara, T. Takeuchi, M. Tabuchi, H. Kageyama, Y. Kobayashi, Y. Kurisu, S. Kondo, R. Kanno, J. Electrochem. Soc. 151 (2004) A1539.

[133] L. J. Fu, H. Liu, C. Li, Y. P. Wu, E. Rahm, R. Holze, and H. Q. Wu, Solid State Sci. 8 (2006) 113.

[134] H.J. Kweon, J.J. Park, J.W. Seo, G.B. Kim, B.H. Jung, H.S. Lim, J. Power Sources 126 (2004) 156.

[135] L.J. Liu, L.Q. Chen, X.J. Huang, X.Q. Yang, W.S. Yoon, H.S. Lee, J. McBreen, J. Electrochem. Soc. 151 (2004) A1344.

[136] M. D. Groner, J. W. Elam, F. H. Fabreguette, and S. M. George, Thin Solid Films 413 (2002) 186.

[137] G. T.K. Fey, H.M. Kao, P. Muralidharan, T.P. Kumar, Y.D. Cho, J. Power Sources 163 (2006) 135.

[138] M. D. Groner, F. H. Fabreguette, J. W. Elam, and S. M. George, Chem. Mater. 16 (2004) 639.

[139] J. W. Elam and S. M. George, Chem. Mater. 15 (2003) 1020.

[140] J. Fu, Y. Baia, C. Liu, H. Yu, Y. Mo, Mater. Chem. Phys. 115 (2009) 105.

[141] A. C. Dillon, A. W. Ott, J. D. Way, and S. M. George, Surf. Sci. 322 (1995) 230.

[142] A. Yamada, B. S. Sang, and M. Konagai, Appl. Surf. Sci., 112 (1997) 216.

[143] E. B. Yousfi, J. Fouache, and D. Lincot, Appl. Surf. Sci., 153 (2000) 223.

[144] C. Delmas, in: F.G. Pistoia (Ed.), Lithium Batteries-New Materials, Developments and Perspectives, Elsevier, New York, 1994, Chap. 12.

Vita

Chuan Cai was born in Luan, Anhui, P. R. China, in 1986. He received his Bachelor of Science degree in material science and engineering from University of Science and Technology of China in Hefei, P. R. China, in July 2008. Then, he entered the Louisiana State University in spring 2009.